DRAFT VERSION AUGUST 17, 2026
Typeset using LaTeX **twocolumn** style in AASTeX63

arXiv:2608.14048v1 [astro-ph.IM] 14 Aug 2026

`Aether.jl`: A High-Performance 3D MHD and Multifluid Dust Code Written in a Dynamic Language with an Interactive Human-AI Development Framework

KA WAI HO[1]

[1] *Kavli Institute for Theoretical Physics, University of California, Santa Barbara, CA 93106, USA*

ABSTRACT

We present `Aether.jl`[a)], a new finite-volume code for compressible hydrodynamics and magnetohydrodynamics, written in Julia and primarily designed for GPU systems. The code solves the MHD equations with constrained transport in Cartesian, cylindrical, and spherical-polar coordinates, using standard high-order Godunov methods. An arbitrary number of dust fluids can be coupled to the gas through stiff mutual drag. It was developed from scratch with interactive Human-coding agent workflow; the paper documents the framework of this workflow alongside the numerical methods. Performance-critical kernel is written through `KernelAbstractions.jl`, and supports runs on CPUs and GPUs from multiple vendors. `Aether.jl` can be ran either from an interactive notebook or batch scripts, keeping prototyping, production runs, and analysis in a single language. We verify the implementation through a series of hydrodynamic, MHD, and dust tests. Although written in a dynamic language, `Aether.jl` achieves comparable or even higher single-GPU throughput than C++ code on the same hardware. In weak scaling on Frontier, parallel efficiency stays above 93% on 4096 GCDs. These results show that a dynamic language now supports production astrophysical MHD simulations on exascale systems. `Aether.jl` and its Jupyter notebook example suite are publicly available.

Keywords: Computational methods (1965), Magnetohydrodynamical simulations (1966), Hydrodynamical simulations (767), Astronomy software (1855)

1. INTRODUCTION

Grid-based fluid and magnetohydrodynamics (MHD) codes form part of the core infrastructure of modern astrophysics. Over the past three decades, community codes such as ZEUS (Stone & Norman 1992), FLASH (Fryxell et al. 2000), RAMSES (Teyssier 2002), PLUTO (Mignone et al. 2007), Athena (Stone et al. 2008), Enzo (Bryan et al. 2014), and Athena++ (Stone et al. 2020) have supported research in nearly every subfield of the discipline. Their applications range from planet formation and accretion flows to the interstellar medium, galaxy evolution, and galaxy clusters. Nearly all of these codes are written in static compiled languages: C, C++, or Fortran. Their designs also reflect the CPU clusters of their era, with distributed-memory parallelism through MPI and data structures tuned for per-core cache performance.

However, in the last decade, mainstream supercomputing has moved to heterogeneous architectures in which GPUs supply nearly all of the compute capability. Current exascale systems, including Frontier, Aurora, and El Capitan, follow this design.[1] Efficient use of such machines requires fine-grained parallelism over millions of threads and careful control of data movement between host and device. These requirements motivated a new generation of astrophysical codes designed for GPUs from the outset, including Cholla (Schneider & Robertson 2015), GAMER-2 (Schive et al. 2018), K-Athena (Grete et al. 2021), QUOKKA (Wibking & Krumholz 2022), Parthenon (Grete et al. 2023), IDEFIX (Lesur et al. 2023), and AthenaK (Stone et al. 2026). Several of them achieve portability across GPU vendors through C++ template frameworks such as Kokkos (Trott et al. 2022). These codes modernize the execution model of astrophysical simulation, but they retain the language model of their predecessors.

Staying with static languages preserves a long-standing split in the research workflow, commonly called the two-language problem (Bezanson et al. 2017). Production solvers are written in compiled languages because interpreted execution cannot meet their performance demands. Prototyping, analysis, post-processing, and visualization instead take place in dynamic languages such as Python, MATLAB, and Julia, whose interactive sessions and rich libraries make exploratory work fast. The split carries costs. A scheme validated in a prototype must be rewritten in the production language before it can run at scale. Each translation costs development time and can introduce new errors.

The same division also imposes a steep learning curve. Programming in astronomy now starts with dynamic lan-

Corresponding author: Ka Wai Ho
kawaiho@kitp.ucsb.edu

[a)] https://github.com/MHDFlows/Aether.jl

[1] https://top500.org

guages, most often Python, so a production code may be the first large compiled program a researcher encounters. Before contributing any physics, a newcomer must absorb template-heavy C++, build systems, and GPU programming models. Layers of performance abstraction further obscure the correspondence between the published scheme and its implementation. For many users the production codes therefore remain black boxes, run but never read. An ideal workflow would keep prototyping, production runs, and analysis within a single language and a single environment.

The Julia language was designed to close this gap (Bezanson et al. 2017). Julia pairs a dynamic, mathematical syntax with just-in-time compilation to native machine code through LLVM. Multiple dispatch specializes generic algorithms at compile time, so high-level source can reach the performance of compiled C. The same compilation path extends to accelerators. `CUDA.jl` compiles Julia functions directly into GPU kernels (Besard et al. 2019). `KernelAbstractions.jl` generalizes this model: a single kernel definition targets NVIDIA, AMD, Apple, and Intel devices as well as multithreaded CPUs (Churavy et al. 2021). `MPI.jl` supplies distributed-memory communication, including GPU-aware transfers (Byrne et al. 2021). Production applications built on this stack now run at scale in neighboring fields, notably the ocean model `Oceananigans.jl` (Ramadhan et al. 2020) and the conservation-law framework `Trixi.jl` (Ranocha et al. 2022).A Julia-native, GPU-first finite-volume code for compressible astrophysical MHD is therefore a promising direction that remains open.

The practice of writing scientific software is also changing at the same time. Large language models trained on code (Chen et al. 2021; Austin et al. 2021) now power interactive coding agents that work inside the terminal, such as Claude Code and Codex.[2] These agents already resolve a substantial fraction of real repository issues in benchmarks such as SWE-bench (Jimenez et al. 2024). In an agentic workflow, the developer specifies intent, reviews changes, and makes design decisions, while the agent writes much of the source. How to conduct such a workflow across the lifetime of a large scientific code remains an open question. Numerical solvers demand sustained correctness, physical validation, and long-term maintainability, and none of these follow automatically from code generation. A new code built from an empty repository offers a controlled setting in which to test both the language and the workflow.

We present `Aether.jl`, a finite-volume code for compressible hydrodynamics and ideal MHD that realizes this experiment. The code is written entirely in Julia. It was developed from scratch in an interactive workflow between the author and coding agents. The project therefore asks two questions. First, can a dynamic language deliver the performance and scalability expected of a production astrophysics code on modern GPU hardware? Second, can a human-AI workflow build such a code while preserving the maintainability, readability, and verification discipline that scientific software requires?

This paper documents the design and presents evidence on both questions. We verify the code using a standard suite of hydrodynamic and MHD test problems. Its measured throughput is competitive with contemporary GPU codes.

The remainder of this paper is organized as follows. Section 2 presents the numerical methods. Section 3 describes how these methods are implemented in a dynamic language and the workflow this enables. Section 4 describes the human-AI development framework. Section 5 reports the validation suite. Section 6 reports performance benchmarks. Section 7 demonstrates two production-scale applications. Section 8 summarizes the results and discusses future directions.

2. NUMERICAL METHODS

2.1. *Newtonian Magnetohydrodynamics*

We solve the equations of Newtonian MHD for a compressible, conducting fluid. In units in which the magnetic permeability is unity, they read

$$\frac{\partial \rho}{\partial t} + \nabla \cdot (\rho \mathbf{v}) = 0, \tag{1}$$

$$\frac{\partial (\rho \mathbf{v})}{\partial t} + \nabla \cdot (\rho \mathbf{v}\mathbf{v} - \mathbf{B}\mathbf{B} + P^* \mathsf{I}) = \mathbf{S}_m, \tag{2}$$

$$\frac{\partial E}{\partial t} + \nabla \cdot [(E + P^*)\, \mathbf{v} - \mathbf{B}\,(\mathbf{B} \cdot \mathbf{v})] = S_E, \tag{3}$$

$$\frac{\partial \mathbf{B}}{\partial t} - \nabla \times (\mathbf{v} \times \mathbf{B}) = 0, \tag{4}$$

where ρ is the mass density, $\mathbf{v}$ the velocity, $\mathbf{B}$ the magnetic field, and I the identity tensor. The total pressure $P^* = p + \mathbf{B}\cdot\mathbf{B}/2$ combines the gas pressure p with the magnetic pressure. The total energy density E sums the internal, kinetic, and magnetic contributions,

$$E = \rho e + \tfrac{1}{2}\rho\, \mathbf{v} \cdot \mathbf{v} + \tfrac{1}{2}\mathbf{B} \cdot \mathbf{B}, \tag{5}$$

where e is the specific internal energy. An ideal-gas equation of state, $p = (\gamma - 1)\,\rho e$ with constant adiabatic index γ, closes the system. The momentum source $\mathbf{S}_m$ collects the optional non-ideal terms: gravity, stochastic forcing, and the drag exerted by dust (Section 2.2). The energy source S_E carries the work of those forces together with optically thin cooling and heating. Both vanish for the ideal system; Section 2.7 describes how all source terms are applied.

In addition to the full MHD system described above, `Aether.jl` supports two independent simplifications. An isothermal mode fixes $p = c_s^2\,\rho$ at constant sound speed c_s and omits Equation 3. A hydrodynamic mode sets $\mathbf{B} = 0$, which reduces Equations 1–3 to the Euler equations; such runs allocate no magnetic storage. The four combinations of adiabatic or isothermal closure with hydrodynamics or MHD

[2] https://github.com/anthropics/claude-code; https://github.com/openai/codex

are selected through the equation-of-state type. For robustness near vacuum, every closure enforces a density floor during the conserved-to-primitive conversion; the ideal gas closures additionally enforce a pressure floor and can impose an optional temperature ceiling.

The equations are solved in conservative form. Mass, momentum, and energy advance as cell averages under a finite-volume Godunov scheme: approximate Riemann solvers supply the face fluxes (Section 2.4), and a method-of-lines integrator supplies the time discretization (Section 2.6). The induction equation is discretized separately with constrained transport, which preserves $\nabla \cdot \mathbf{B} = 0$ (Section 2.5).

2.2. *Multifluid Dust*

Dust is modeled as N pressureless fluid species coupled to the gas by linear drag. Each species k carries its own density ρ_k and velocity $\mathbf{v}_k$ and obeys

$$\frac{\partial \rho_k}{\partial t} + \nabla \cdot (\rho_k \mathbf{v}_k) = 0, \tag{6}$$

$$\frac{\partial (\rho_k \mathbf{v}_k)}{\partial t} + \nabla \cdot (\rho_k \mathbf{v}_k \mathbf{v}_k) = \frac{\rho_k (\mathbf{v} - \mathbf{v}_k)}{t_{\mathrm{s},k}}, \tag{7}$$

where $t_{\mathrm{s},k}$ is the stopping time of species k. The drag term accelerates each species toward the gas velocity on that timescale. The gas momentum equation gains the opposite reaction, $-\sum_k \rho_k (\mathbf{v} - \mathbf{v}_k)/t_{\mathrm{s},k}$, so the mixture conserves total momentum. The gas energy equation gains the matching term, chosen so that the energy dissipated by the drift between phases appears as gas heat. The stopping time is specified per species, either as a constant or as a function of position, gas density, dust density, and sound speed. This covers Epstein, constant, and constant-coefficient drag laws (Epstein 1924; Lehmann & Wardle 2018).

Each species advances through the same finite-volume machinery as the gas. The reconstruction schemes are shared, and fluxes come from a pressureless Riemann solver: by default the diffusive Rusanov flux of Krapp et al. (2024, Appendix E), with an HLL variant using signed wave-speed bounds as an alternative. The diffusive default passes robustly through the δ shocks that converging pressureless flow forms. Cells whose dust density falls below a floor are reset to the floor with zero velocity, which keeps evacuated regions from binding the timestep.

The drag coupling is stiff whenever $t_{\mathrm{s},k} \ll \Delta t$, as holds for small grains. `Aether.jl` therefore integrates drag implicitly inside the time integrator, following Krapp et al. (2024). Because every species couples to the gas but not to the other species, the per-cell drag matrix has arrowhead structure and inverts in closed form at cost linear in N. The implicit stage is solved exactly, conserves the total momentum of the system, and remains stable for arbitrarily small stopping times. Section 2.6 describes the surrounding implicit-explicit integrator. Comparable multifluid dust schemes are implemented in FARGO3D (Benítez-Llambay et al. 2019) and Athena++ (Huang & Bai 2022).

2.3. *Mesh, Coordinates, and Boundary Conditions*

`Aether.jl` adopts the MeshBlock domain decomposition introduced by Athena++ (Stone et al. 2020). The computational domain, in one, two, or three dimensions, is divided into logically identical blocks of fixed size. Each block is padded with the maximum ghost width required by its reconstruction and Riemann solver: 1 cell for donor-cell reconstruction, 2 for PLM, and 3 for the PPM-family and WENO schemes; multidimensional LHLLC/LHLLD independently requires at least 2. Blocks are ordered along a Morton space-filling curve and distributed over MPI ranks in contiguous slices of that ordering. The grid is currently uniform and single-level. The block structure is naturally open for a possible future extension of mesh refinement.

The array layout is chosen for GPU parallelism. All cell-centered fields of a rank live in five-dimensional arrays indexed (i, j, k, v, m), where (i, j, k) are the cell indices, v the variable, and m the block. Julia stores arrays in column-major order, so the cell index i varies fastest and consecutive GPU threads touch consecutive memory. The block index is a dimension of the kernel launch itself: one launch advances every block a rank owns. Device utilization is therefore set by the total cell count of the rank rather than by the size of any single block, which keeps small blocks viable as units of decomposition and future refinement.

Three coordinate systems are supported, Cartesian (x, y, z), cylindrical (R, ϕ, z), and spherical-polar (r, θ, ϕ), each with uniform spacing in every coordinate. Geometry enters the solver only through exact face areas, cell volumes, edge lengths, and volume-weighted cell centroids. These factors are evaluated on demand by coordinate-specialized functions instead of being stored in arrays. The momentum source terms required in curvilinear coordinates are described in Section 2.7.

Ghost cells are filled by one exchange that covers all face, edge, and corner neighbors, up to 26 per block in three dimensions, as constrained transport requires. Neighbors on the same rank copy block to block; remote strips are grouped by peer rank, yielding at most one send and one receive per peer in each exchange. Physical boundary conditions are imposed after the exchange. Built-in choices are periodic, outflow, reflecting, and a polar condition for the spherical axis, together with user-defined conditions. The polar condition fills axis ghost zones from the cells half a turn away in azimuth, with the sign flips and the face-field and axis electric-field treatment that MHD requires.

2.4. *Reconstruction and Riemann Solvers*

Within each block the conservative equations are discretized in integral form. For a cell of volume V the cell-averaged state $\bar{U}$ evolves as

$$\frac{d\bar{U}}{dt} = -\frac{1}{V} \sum_f A_f \, \hat{F}_f + \bar{S}, \tag{8}$$

where the sum runs over the faces of the cell, A_f is the face area, $\hat{F}_f$ is the outward-directed numerical flux through that face, and $\bar{S}$ collects source terms (Section 2.7). Because A_f

and V are the exact geometric quantities, Equation 8 applies unchanged in all three coordinate systems. Fluxes are evaluated from the current stage state, and temporal accuracy comes from the Runge-Kutta integrator (Section 2.6).

Numerical fluxes are computed direction by direction. Along each direction, cell-centered primitive variables are reconstructed to the left and right sides of every face. Six base schemes are available: piecewise-constant donor cell; a piecewise-linear method (PLM) with the monotonized harmonic-mean limiter of van Leer (1974); the piecewise-parabolic method (PPM; Colella & Woodward 1984); PPM5, which limits a 5 point 4th-order upwind-biased interface value with the unmodified PPM limiter; 5th-order WENO-Z (Borges et al. 2008); and the adaptive-order WENO-AO(5,3) of Balsara et al. (2016). WENO-AO hybridizes the quartic over the full 5 cell stencil with 3 quadratic sub-stencils. Smooth flow recovers the quartic, including at the extrema where PPM clips; discontinuities reduce the scheme to a 3rd order WENO of the sub-stencils. For the energy-evolving closures, both WENO schemes also come in variants augmented with the positivity-preserving rescaling of Zhang & Shu (2010). The nonlinear weights of both WENO schemes use a scale-invariant regularization in place of the customary fixed constant, so they respond identically at every amplitude and remain well behaved in single precision. Reconstruction acts componentwise on primitive variables. In MHD the cell-centered magnetic field is reconstructed alongside them; the positivity-limited variants reconstruct the field with PPM instead, because overshoots in $\mathbf{B}$ can seed oscillatory induction fluxes.

The reconstructed states are rotated into the frame of each face and passed to an approximate Riemann solver. For hydrodynamics the options are Rusanov, HLLE (Harten et al. 1983; Einfeldt 1988), and HLLC (Batten et al. 1997; Toro 2009). For MHD the options are Rusanov, HLLE, and HLLD (Miyoshi & Kusano 2005). HLLC and HLLD also come in the low-dissipation variants LHLLC and LHLLD of Minoshima & Miyoshi (2021), which rescale the pressure dissipation of the contact wave with the local Mach number and suppress the numerical shock instability at grid-aligned shocks. Section 5.7 quantifies the low-Mach behavior. Isothermal counterparts exist for every solver except HLLC and LHLLC; the isothermal HLLD follows Mignone (2007).

2.5. *Constrained Transport*

The primary representation of the magnetic field is the set of area-averaged normal components on cell faces. Cell-centered values, needed for reconstruction and for the total energy, are averages of the two bounding faces. The face field advances by constrained transport (Evans & Hawley 1988), which discretizes the induction equation in integral form. Each face average $\bar{B}_f$ obeys

$$\frac{d\bar{B}_f}{dt} = -\frac{1}{A_f}\oint_{\partial f} \mathbf{E}\cdot d\boldsymbol{\ell}, \tag{9}$$

where $\mathbf{E} = -\mathbf{v}\times\mathbf{B}$ is the electric field and the circulation is a signed sum of edge-centered electric fields weighted by exact edge lengths. Every edge is shared by two faces of any given cell, and their circulations traverse it in opposite senses. The discrete magnetic flux leaving each cell is therefore constant in time. As a result $\nabla\cdot\mathbf{B} = 0$ holds in every supported coordinate system (cf. Tóth 2000), and the induction equation needs no geometric source terms. The face field carries its own register pair and joins the stage combinations of Section 2.6.

The edge electric fields derive from the Riemann fluxes. In the face-frame Riemann problem the normal magnetic field takes the stored face value on both sides, and the tangential components of the resulting induction flux are face-averaged electric fields. The four face values around each edge are combined with the upwind averaging of Gardiner & Stone (2005, 2008), which selects gradient corrections by the direction of mass flux across the intervening faces. On meshes that include the spherical axis, the axis-aligned electric field is replaced by its azimuthal mean.

2.6. *Time Integration*

Explicit time integration uses Runge-Kutta methods in the two-register, low-storage form of Ketcheson (2010). Only two copies of the conserved state exist, whatever the stage count. Writing the registers as u_1 and u_2, stage l performs

$$\begin{aligned} u_2 &\leftarrow u_2 + \delta_l\, u_1, \\ u_1 &\leftarrow \gamma_{0,l}\, u_1 + \gamma_{1,l}\, u_2 + \beta_l\, \Delta t\, L(u_1)\,, \end{aligned} \tag{10}$$

where L is the discrete right-hand side of Equation 8 and $(\gamma_{0,l}, \gamma_{1,l}, \beta_l, \delta_l)$ are the coefficients of the chosen method. Three integrators are provided. `RK2` and `RK3` are the optimal two-stage second-order and three-stage third-order strong-stability-preserving schemes (Gottlieb et al. 2009); both have unit Courant limit. `RK4` is the four-stage fourth-order low-storage method of Ketcheson (2010), with Courant limit 1.39.

Stiff drag terms are integrated with the second-order implicit-explicit scheme `IMEX2P`, the two-solve IMEX pair of Ascher et al. (1997) on which Krapp et al. (2024) build their multifluid drag solver. Its explicit part is a two-stage scheme in the same two-register form; its implicit part is diagonally implicit, stiffly accurate, and L-stable. Each step applies exactly two of the closed-form drag solves of Section 2.2, one per stage, with implicit weight $\lambda\,\Delta t$, where $\lambda = 1 + 1/\sqrt{2}$. This choice keeps every explicit combination weight nonnegative; the admissible Courant fraction of the explicit part becomes $1/\lambda \approx 0.586$. With no stiff term attached, `IMEX2P` reduces to its explicit part exactly. Drag is woven into the stages rather than operator split because splitting fails to reach the correct drift equilibrium when external forces act (Appendix C of Krapp et al. 2024).

The timestep follows from the fastest signal speed crossing each cell. After every cycle the code evaluates

$$\Delta t = C\, C_{\max} \min_{\text{cells}} \min_{d} \frac{\Delta x_d}{|v_d| + c_d}, \tag{11}$$

where Δx_d is the physical cell width along direction d (an arc length in curvilinear coordinates) and v_d is the flow velocity along d. The signal speed c_d is the sound speed in hydrodynamics, the directional fast magnetosonic speed in MHD, and zero for pressureless dust. The factor $C_{\max}$ is the stability limit of the chosen integrator, and the Courant factor $C \in (0, 1]$ sets the fraction of that limit to run at, with default $C = 0.3$. Because the minimum is taken per direction rather than summed over directions, multidimensional runs typically use $C \approx 1/n_{\dim}$. Source terms may declare local timescales that enter the same reduction; the drag adds no constraint because it is implicit.

2.7. *Source Terms*

`Aether.jl` designed a flexible framework for cell-centered source terms. Cell-centered source terms beyond the ideal fluxes enter through three common integration slots: unsplit terms act within the Runge-Kutta stages, split terms after the stage loop, and driving terms before it.

Pointwise sources are functions of position, time, and the local primitive state of every fluid; each returns rates of change for the conserved variables it affects. Built-in pointwise packages and user-defined terms take this form, while components that need face fluxes, global reductions, or nonlinear solves implement the same slots directly. Each slot serves a different class of process, ansd the built-in packages illustrate the match. A source may also declare a local timescale, which then enters the timestep reduction of Equation 11.

Unsplit sources, the default, are added at every Runge-Kutta stage with the same stage weight $\beta_l \, \Delta t$ as the flux divergence, so time-independent, state-dependent sources participate in the full-order Runge-Kutta update; explicitly time-dependent rates are currently evaluated at the cycle-start time because stage abscissae are not tracked. All unsplit sources fuse into one kernel, which gathers the local state once and accumulates every rate before storing. This mode fits forces that are smooth on the step and should track the flow through every stage.

The curvature terms of cylindrical and spherical-polar coordinates are applied unsplit at every stage. `Aether.jl` builds them from the total stress tensor

$$T_{ij} = \rho \, v_i v_j + P^* \delta_{ij} - B_i B_j, \tag{12}$$

whose divergence in curvilinear coordinates produces the momentum sources, for example $\rho v_\phi^2 / R$ in cylindrical geometry; hydrodynamics is the $\mathbf{B} = 0$ case of the same expression. The discrete factors of these sources are the same face areas and cell volumes as the flux divergence, so a uniform medium at rest stays at rest to machine precision. The terms attach automatically on curvilinear meshes and apply in pressureless form to each dust species.

Split sources apply once per step, after the stage loop, as a single first-order operator-split update over the full Δt. The mode gives up temporal order in exchange for stability and cost, and an optional interval super-cycles a term over several steps with the accumulated weight.

Driving sources apply once per step, before the integrator begins, so the injected field stays frozen across the stages of that step. This slot serves stochastic forcing, for which the built-in turbulence driver is the model case. It forces the large-scale Fourier modes of a periodic box with an Ornstein-Uhlenbeck process of prescribed correlation time (Eswaran & Pope 1988; Schmidt et al. 2009). A Helmholtz projection of the mode amplitudes sets the solenoidal fraction of the forcing. Each kick subtracts the mean acceleration, so no net momentum enters, and rescales the amplitude so the injected energy matches the prescribed power exactly. Kicks may be applied every step or accumulated into impulses at a fixed driving interval.

In addition, magnetic sources can be entered as user-defined electric fields added at cell edges inside the constrained-transport update, which preserves $\nabla \cdot \mathbf{B} = 0$ by construction. For Dust-Gas coupling, as described in Section 2.6, stiff drag bypasses the source handler altogether: it is integrated by the implicit stages of `IMEX2P`.

2.8. *Dual-Energy Formalism*

Supersonic and strongly magnetized flows store nearly all of their energy in kinetic and magnetic form, which makes the total energy an ill-conditioned source for the thermal pressure. Recovering the internal energy from Equation 5 then subtracts nearly equal numbers, so the truncation error of the scheme can become comparable to the internal energy itself. Since pressure forces are negligible in exactly these regions, the error leaves the dynamics unaffected. Nevertheless, whenever the temperature itself is required (e.g., for chemistry or radiative cooling), a remedy is needed. For these regimes `Aether.jl` implements the dual-energy formalism of Bryan et al. (1995), in the entropy form adopted by GAMER-2 (Schive et al. 2018).

The formalism evolves a modified entropy density alongside the total energy. In smooth adiabatic flow it obeys

$$\frac{\partial S}{\partial t} + \nabla \cdot (S \, \mathbf{v}) = 0, \qquad S = \frac{p}{\rho^{\gamma - 1}}, \tag{13}$$

so the pressure follows from S and the density alone, with no subtraction. At shocks the physical entropy jumps while Equation 13 does not, so the advected value is trusted only where dissipation is absent. In the discrete update, S is carried as a passively advected scalar. Every Riemann solver leaves its dynamical flux unchanged and adds an entropy flux equal to the mass flux times the entropy per unit mass, S/ρ, of its upwind side (Larrouturou 1991).

The total energy and the advected entropy now provide two estimates of the pressure, and the conserved-to-primitive conversion chooses between them cell by cell. The selection uses the ratio of the recovered internal energy to the kinetic plus magnetic energy (kinetic alone in hydrodynamics), which controls the relative error of the subtraction. Below a threshold α_{switch} (10^{-3} by default) the subtraction is no longer trusted: the internal energy comes from the entropy, $\rho e = S \rho^{\gamma - 1} / (\gamma - 1)$, and the stored total energy is

rewritten to match. Above a second threshold $\alpha_{\rm sync}$ (10^{-1} by default) the subtraction is accurate, so the conservative value stands and S is resynchronized from it. This resynchronization alone carries shock heating into the entropy, so no separate shock detector is needed. Between the thresholds the conservative energy still sets the pressure but S is left untouched. The entropy is thus written only where the subtraction is accurate and read only where it has failed, so its error never returns to the pressure.

3. IMPLEMENTATION IN A DYNAMIC LANGUAGE

In this section we describe how features native to a dynamic language shape the implementation of `Aether.jl` as a production solver. Rather than adopting an architecture inherited from established static-language codes, we organize each part of the program around a focused Julia abstraction. Our goal is to retain the performance required for production calculations while keeping the implementation concise and intuitive. The same principle governs both the computational core—numerical specialization, portable CPU/GPU kernels, and distributed communication—and the user-facing layers for problem setup and data output. Sections 3.1 through 3.3 present the computational components, while Sections 3.4 and 3.5 describe the user-facing interface and output system.

3.1. *Multiple Dispatch*

Scientific simulation codes must support many combinations of physical models, numerical schemes, boundary treatments, and hardware backends. In conventional Fortran or C implementations, these choices are often selected through `if/else` branches or preprocessor flags such as `#ifdef`. As features accumulate, branches spread into inner loops, build configurations multiply, and the active code path becomes difficult to trace. This complexity contributes to the accessibility barrier discussed in Section 1. `Aether.jl` instead uses what we call implicit propagation. The user specifies each choice once, for example by passing `RK3()` or `HLLD()` to a constructor, and Julia specializes every routine that depends on it. The source therefore requires neither repeated bookkeeping nor runtime branches. The remainder of this subsection explains how multiple dispatch and compilation make this propagation possible.

Julia's multiple dispatch provides the mechanism behind this implicit propagation. A Julia function can have several methods, and the method used for a particular call is selected from the types of all its arguments (Bezanson et al. 2017). In `Aether.jl`, each interchangeable simulation component, such as a reconstruction scheme, Riemann solver, equation of state, or time integrator, is represented by a distinct Julia type. Values such as `WENOZ()`, `HLLD()`, and `RK3()` therefore identify both the user's choice and the methods that implement it. When one of these values is passed to a numerical routine, Julia automatically selects the matching method. Replacing a component consequently changes every routine that dispatches on its type without changing the corresponding call sites. Construction then carries these type-based choices through the full solver.

The `Simulation` constructor does this by encoding the selected components as type parameters, so each combination of equation of state, reconstruction scheme, Riemann solver, and time integrator gives the simulation a distinct concrete type. When `run!` is called for the first time, Julia compiles the methods required by that type into machine code. The resulting kernels contain only the selected algorithms, so their inner loops need no runtime branches to determine which configuration is active. The type information also exposes unsupported combinations before the physical state is advanced. For example, pairing HLLC with an isothermal equation of state raises a missing-method error because no HLLC method is defined for that closure (Section 2.4).

This specialization is not limited to numerical schemes. Geometry-dependent operations dispatch on the coordinate type of the `Mesh`, allowing the same update kernels to work in every coordinate system introduced in Section 2.3. On a spherical-polar mesh, for example, the cell volume used in Equation 8 is $\frac{1}{3}\left(r_+^3 - r_-^3\right)\left(\cos\theta_- - \cos\theta_+\right)\Delta\phi$. The azimuthal cell width used in Equation 11 is $r\sin\theta\,\Delta\phi$. On a Cartesian mesh, the same methods return constant grid spacings, which the compiler folds into the compiled kernels. Selecting the coordinate system at mesh construction therefore supplies the correct geometric factors throughout the solver without modifying the update kernels or adding geometry-dependent branches. Each compiled kernel contains only the geometry operations selected by the mesh type, so support for the other coordinate systems adds no cost to that run.

The multiple-dispatch design also makes the cost of extension predictable. Adding a Riemann solver requires only a new type and one method. No existing kernel, driver, or configuration file needs to change, and no new `if` branch is added to select the solver. Multiple dispatch selects the method whenever its type appears in a configuration, and the compiler specializes the resulting kernel. Each scheme therefore remains localized in the source as one type and its methods, keeping the implementation close to the published algorithm.

3.2. *XPU Kernels*

The pressure behind this layer comes from the hardware, where nearly all compute capability now sits in GPUs and each vendor exposes it through a different programming model: CUDA for NVIDIA, HIP for AMD, SYCL for Intel. Writing kernels in one of these models ties the code to one vendor, and maintaining several kernel sets multiplies the work. The established C++ solution is the template framework Kokkos (Trott et al. 2022), which lets one kernel source compile for multiple hardware vendors. K-Athena, Parthenon, IDEFIX, and AthenaK all use Kokkos to provide this performance portability (Grete et al. 2021, 2023; Lesur et al. 2023; Stone et al. 2026). Kokkos thus solves the portability half of our problem. The remaining half is language: we want the same write-once kernels expressed in plain Julia, inside the single-language workflow that motivates this

project. The plain language buys us flexibility in return: a kernel stays an ordinary Julia function, which composes with the dispatch of Section 3.1 and can be read, modified, and tested interactively like the rest of the code.

Julia provides this machinery through native compilation. `CUDA.jl` established that the language compiler can emit GPU kernels directly from Julia functions (Besard et al. 2019). `KernelAbstractions.jl` generalizes that capability into a portability layer (Churavy et al. 2021): a kernel written once against its interface compiles to NVIDIA CUDA, AMD ROCm, Intel oneAPI, and Apple Metal devices, as well as to multithreaded CPU code. Because the abstraction lives inside the language, kernels keep the plain syntax of the surrounding source.

Every performance-critical loop in `Aether.jl` is written against this layer, so one code path serves every architecture. The user selects an execution backend when constructing the mesh, and that choice becomes part of the mesh's concrete type. Passing `CPU()` allocates the state arrays in host memory and runs the kernels with multithreaded CPU execution. Passing `GPU(CUDABackend())` instead allocates the arrays in NVIDIA GPU memory and compiles the same kernel functions for CUDA; corresponding backend wrappers target devices from the other vendors. Array allocation and kernel launch dispatch on this backend type, so the numerical algorithms and their call sites contain no architecture-specific branches.

Nearly every computational kernel traverses the mesh data through one of two helper functions. `for_each!` applies an operation independently to every cell in every block owned by an MPI rank; a single kernel launch spans the three cell indices and the block index. `map_reduce` performs a similar traversal while combining the resulting values, for example to find the timestep minimum in Equation 11 or compute volume integrals for history output (Section 3.5). These two helpers centralize launch configuration, index calculations, and bounds handling, leaving each computational kernel to specify only the operation performed on the data.

The traversal helpers and multiple dispatch together collapse the entire family of Godunov flux kernels into the roughly ten lines shown in Figure 1. This single body covers every direction, reconstruction scheme, Riemann solver, equation of state, and execution backend. It states only the three operations common to all configurations: reconstruct the two face states, solve the Riemann problem in the face frame, and store the flux. `for_each!` supplies the backend-independent traversal and launch machinery, while dispatch selects the appropriate implementations of reconstruction, frame transformation, and the Riemann solve. Because these choices are encoded in concrete types (Section 3.1), the compiler specializes this compact, general source into code as concrete as a kernel written by hand for one particular configuration.

Backend portability follows from the same design. The CPU and GPU backends compile the same kernel body, so a kernel can be developed and debugged on the CPU, where standard tooling applies, and then run unchanged on a GPU.

```
for_each!(architecture, ri, rj, rk,
          1:nblocks; workgroup) do i, j, k, m
    wl, wr = face_states(scheme, dir,
                         W, i, j, k, m, nv)
    f = riemann_flux(solver, eos,
                     to_face_frame(dir, wl),
                     to_face_frame(dir, wr))
    store_state!(F, from_face_frame(dir, f),
                 i, j, k, m)
end
```

Figure 1. The actual code of the flux kernel of the Godunov update in the `Hydro` module. `for_each!` maps the body over the cell ranges `ri`, `rj`, `rk` and all blocks of the rank, launching on the selected `architecture` with the given `workgroup` size (Section 2.3). The body reconstructs the two face states from the primitive array `W`, solves the Riemann problem in the face frame, and stores the flux in `F`. Because `scheme`, `solver`, and `eos` are the compile-time types of Section 3.1, this one body serves every direction, reconstruction scheme, Riemann solver, equation of state, and backend.

3.3. *Parallelism*

Message passing remains the portable substrate for distributed memory on production clusters, and `Aether.jl` adopts it directly. `MPI.jl` wraps the system MPI library in a native Julia interface with negligible overhead (Byrne et al. 2021). Each MPI rank owns a contiguous slice of the Morton-ordered block list (Section 2.3) and, on GPU systems, drives one device.

Communication is confined to three operations. Ghost-zone exchange fills block boundaries with one message per pair of off-rank neighbors, as described in Section 2.3. The timestep of Equation 11 completes with one global reduction per cycle. The history diagnostics of Section 3.5 reduce their sums and extrema, conserved totals such as mass and the maximum $|\nabla \cdot \mathbf{B}|$, across ranks before rank zero writes. Every other operation in the solver is local to a rank. Monitoring conservation on the fly therefore costs one scalar reduction per output.

On GPU systems the exchanged data lives in device memory. With a GPU-aware MPI library, `MPI.jl` hands device buffers to the library directly, so messages move between GPUs without a staging copy through the host (Byrne et al. 2021).

In addition, we noted that the small-scale parallelism does not have to go through MPI: the XPU kernels support multithreading through `KernelAbstractions.jl`, so a single node with many CPU cores runs without `MPI.jl`.

Beyond one node, the same code runs under `mpiexec` on a cluster (Section 3.4). The narrow communication interface keeps both modes on one code path. The scaling of this design is quantified in Section 6.

3.4. *User Interface, Problem Setup, and Execution Modes*

The abstractions described above also define the user interface of `Aether.jl`. Their practical value is that even a complicated numerical experiment can be expressed con-

```
using AEther

γ  = 5 / 3
B0 = 1 / sqrt(4π)

A(x, y, z) = (0, 0, B0 * (cos(4π * x) / 4π +
                          cos(2π * y) / 2π))

w(x, y, z) = (25 / (36π),            # density
              -sin(2π * y),          # v1
              sin(2π * x),           # v2
              0,                     # v3
              5 / (12π) / (γ - 1))   # int. energy

mesh = Mesh(CPU(); size = (256, 256, 1),
            extent = (1, 1, 1),
            cells_per_block = (64, 64, 1),
            nghost = 3)

sim = Simulation(mesh;
                 eos = IdealMHD(γ, 1e-12, 1e-10),
                 reconstruction = WENOZ(),
                 riemann_solver = HLLD(),
                 stepper = RK3(),
                 cfl = 0.4)

set_initial_condition!(w, sim;
                       vector_potential = A)

run!(sim; stop_time = 0.5)
```

Figure 2. Complete `Aether.jl` setup of the Orszag-Tang vortex: an ideal-MHD run on a 256^2 grid with WENO-Z reconstruction, the HLLD Riemann solver, and third-order Runge-Kutta integration. Loading `CUDA.jl` and replacing `CPU()` with `GPU(CUDABackend())` runs the same script on a GPU.

cisely in the same vocabulary used to describe its physics and numerical methods. Traditional simulation codes often distribute problem setup between a parameter file and a problem-generator source file, which must be edited and recompiled for customized experiments. `Aether.jl` is instead used as a Julia library. Users define the initial state and custom physics as ordinary functions, assemble a `Mesh` and a `Simulation` through constructors, and call `run!`. No separate parameter parser, problem-generator registry, or build step stands between the mathematical specification and the code that is executed.

Figure 2 demonstrates this design with the Orszag–Tang vortex (Orszag & Tang 1979). The complete setup and launch contain only 9 lines of Julia code. The functions `w` and `A` directly state the primitive variables and magnetic vector potential of the initial condition. The `Mesh` constructor specifies the domain, resolution, block decomposition, and execution backend, while the `Simulation` constructor selects the equation of state, reconstruction scheme, Riemann solver, and time integrator. The final two statements initialize the state and advance it to the requested time. No prewritten Orszag–Tang problem generator is invoked; all problem-specific information appears in the listing. Its brevity therefore comes from composing general interfaces rather than hiding configuration elsewhere.

The same problem description operates in three settings. It can be pasted into the Julia REPL for interactive execution, placed in a Jupyter notebook together with analysis and visualization, or launched as `mpiexec -np 8 julia script.jl` under a cluster batch scheduler. The physical and numerical specification remains unchanged across these modes. Scaling a prototype into a production run requires changing only the mesh or backend arguments and the launch command, rather than translating the problem into another language or a compiled source module.

Because `Aether.jl` is a library rather than a separate executable, the `Simulation` object remains accessible after `run!` returns, and its fields are ordinary Julia arrays. A user can inspect slices, compute diagnostics, and visualize the state in the same process that performed the simulation. The script that defines the problem therefore also serves as an executable record of the experiment and as the starting point for its analysis. This continuity removes the translation step of the two-language workflow described in Section 1.

Concision does not restrict problem-specific physics. User-defined boundary conditions attach as Julia functions (Section 2.3), source terms use the interface of Section 2.7, and custom diagnostics enter through the history columns of Section 3.5. A complete experiment, including its parameters, custom physics, execution settings, and analysis, can therefore remain in one version-controlled Julia file. The following subsection describes how field and restart output extend this workflow to data stored on disk.

3.5. *Output and Restart*

Output is handled by `Output` structs attached to the simulation at construction and scheduled inside `run!`. Three writers cover the standard needs. `HistoryOutput` appends volume-integrated diagnostics to a text file written by rank zero: total mass, momentum, and energy, the maximum $|\nabla \cdot \mathbf{B}|$ for MHD, and user-defined sum, minimum, or maximum columns. Conservation and stability can therefore be monitored while a run executes. `FieldOutput` writes selected primitive, conserved, or derived fields, such as vorticity or current density, in single precision by default. `RestartOutput` writes the complete state that continues a run, at working precision.

The `Output` checks the simulation time after every cycle and fires when the time exceeds the next scheduled dump. The history writer can also fire on cycle counts, and the restart writer on elapsed wall-clock time, which protects long runs against batch queue limits. A forced dump completes every sequence at the stop time, so the final state always reaches disk.

To handle the output efficiently, Field and restart data are written through ADIOS2 (Godoy et al. 2020) using its BP5 engine. ADIOS2 was developed within the United States Exascale Computing Project and handles production output for simulation codes at leadership-class facilities. Adopting it delegates parallel writing, aggregation, and format evolution to an established library. A dump stores every variable as one array in global cell space, and ADIOS2 aggregates the

writes within each node. Analysis tools therefore address the domain directly, which is the access pattern uniform-grid analysis needs.

In addition, each file is self-describing. Alongside the arrays it also carries meta data such as mesh-level and version attributes, so a reader reconstructs the grid without access to the generating script. The same metadata leaves room for growth: for example, the mesh refinement (Section 2.3) extends the format with few modifications. Because ADIOS2 provides Julia and Python bindings, the files open directly in the environments where analysis happens.

4. HUMAN-AI DEVELOPMENT FRAMEWORK

Developing and verifying a production simulation code has historically demanded years to decades of sustained effort, and that cost shapes what a small research group can attempt. Interactive coding agents, such as Claude Code and Codex, have changed this situation within the past two years. Working directly inside a repository, they implement multi-file changes from natural-language specifications and resolve a substantial fraction of real software issues (Jimenez et al. 2024; Yang et al. 2024). Their arrival changes the economics of building scientific software, yet leaves its obligations intact: correctness, maintainability, and validation must still be earned. Whether a human-AI collaboration can sustain those obligations over the multi-year lifetime of a solver, rather than over a single task, remains an open question. `Aether.jl` was built as a deliberate experiment on this question, and this section documents the workflow that resulted.

The central challenge in this experiment is the gap between bounded-task performance and sustained software development. Current coding agents are effective on tasks that can be completed within one working session, such as generating a small program or implementing a localized change. We refer to this as one-shot code generation: although the agent may take many steps within the session, its project-specific context and the lessons learned during the task do not need to persist afterward. A production simulation code poses a different problem. Its development spans many tasks, sessions, and model versions, while its architecture, conventions, and accumulated lessons must remain coherent throughout.

This difference creates three problems. First, project knowledge does not automatically persist between sessions. Each new session receives only the project-specific information supplied in its context and must otherwise rediscover the state of the code, its module structure and conventions, and the reasoning behind earlier design decisions. Second, agents and model versions differ in their preferences for naming, abstraction, and implementation style. Without shared standards, changes accumulated across many sessions would gradually make the codebase inconsistent. Third, corrections made in one session do not automatically influence the next. Characteristic errors can therefore recur unless lessons from human intervention are recorded as explicit guidance for future sessions. Together, these problems define what a sustained development workflow must provide.

We propose the development workflow used for `Aether.jl` as one answer to these problems. Its central idea is to externalize three forms of information that must persist across sessions: project knowledge, shared standards, and accumulated lessons. These are stored as version-controlled markdown documents alongside the source. To make this project memory available to each agent, the workflow uses configuration mechanisms provided by modern agent harnesses. A harness is the tool that connects a language model to a working repository; Claude Code and Codex are examples. It can load a designated instruction file into every session, apply rule files scoped to the paths being edited, and retrieve task-specific procedural documents, or skills, on demand. `Aether.jl` organizes its project memory around these mechanisms (Section 4.1). It uses a bounded session discipline to separate design decisions from implementation (Section 4.2) and records each code change through a pre-commit hook (Section 4.3). The same framework also supports scientific use of `Aether.jl`. An agent can draw on the project memory and operational skills to help users configure, test, and launch simulation problems (Section 4.4). Because these documents reside in the repository rather than in a particular harness, the workflow remains tool-agnostic: any agent that can read them can follow it.

The documents serve two audiences at once. Human developers and users read the same files: the project map orients a new contributor, the skills double as a quick-start guide, and the design documents give the overview a reader wants before opening the source. Developers and agents maintain this memory through the feedback loop described below. Users can also benefit from it through an agent, which applies the project knowledge and operational skills when helping them configure and run simulations.

4.1. *Markdown File System*

Within this workflow, the repository serves as durable project memory, but not every document belongs in every agent session. `Aether.jl` therefore assigns each markdown document a specific purpose and a rule for when it enters an agent's context. As Table 1 summarizes, the project map is loaded at the start of every session; scoped rules, skills, and design documents enter only when relevant to the task; and the session journal is written before each commit and consulted during audits. Because all these files are version-controlled alongside the source, project memory travels with every clone, remains synchronized across machines and collaborators, and evolves under the same review as the code.

`AGENTS.md` serves as the entry point: a map of the repository rather than a manual. It answers at the start of every session what an agent would otherwise rediscover by exploring: what the package is, the layout and role of every directory, and the commands that set up the environment and run the tests. It also states the core design rules (dispatch over branching, code that reads as math, backend-agnostic kernels; Section 3), so a session follows the project's conventions from its first line instead of the model's defaults.

Table 1. The markdown file system that carries project memory across agent sessions. Every file evolves with the code except the session journal, which is append-only. The same top-level file answers to the names `AGENTS.md` and `CLAUDE.md`, the conventions different harnesses search for.

Files	Contents	Enters an agent's context
`AGENTS.md`	project map: layout, commands, core rules	always, at session start
`.claude/rules/`	scoped rulebooks: naming, kernels, tests, docs	when editing a file in the rule's scope
`.claude/skills/`	procedures: environments, problem runs, cluster jobs	on demand, when the task matches
`dev/design-*.md`	module designs: decisions, interfaces, rejected alternatives	at task start, for the modules touched
`dev/log/`	session journal: prompts, interventions, lessons	written before every commit; read for audits

For each detailed topic it points to a scoped rulebook instead of inlining the rules. A budget keeps the file below 150 lines, because this document occupies every context window and must not crowd out the task itself.

The rulebooks under `.claude/rules/` carry the uniform quality control that the second problem above demands. Seven files, about 300 lines in total, govern naming and comment discipline, kernel writing, docstrings, testing, documentation, examples, and interactive execution. Each file declares in its header the paths it governs. The harness loads the file whenever the agent edits a matching path. If the harness lacks this mechanism, `AGENTS.md` instructs the agent to read the matching rulebook before editing. For example, the kernel rulebook requires type-stable and allocation-free kernel bodies, forbids hard-coded `Float64` literals, and prefers `ifelse` to branching (Section 3.2). Because the rules bind at the file level rather than the session level, every model that touches `src/` writes kernels under the same constraints, whatever its native style.

Skills under `.claude/skills/` describe how to use the code rather than how to write it. Each skill packages one operational procedure: constructing a scratch environment and launching a test problem on CPU or GPU, serial or under MPI, or running multi-node GPU jobs, with launch patterns and verified baselines. The harness loads a skill only when the task matches its stated description, so the context cost is paid on demand. Rediscovering such operational knowledge by trial costs an agent most of a session, and a single read replaces that exploration. The same pages give human users a quick-start guide and supply the procedures used by the agent-assisted workflow of Section 4.4.

The design documents `dev/design-*.md`, a cross-module overview plus one file per module, separate decision-making from implementation. Each document is written during the design session of Section 4.2 and serves as the contract for the implementation; afterward it is updated to describe the module as built. It records interfaces, data layouts, and decisions with their reasons, together with the alternatives that were rejected. Recording rejections proved as important as recording decisions, because agents repeatedly re-propose plausible ideas that have already failed. The boundary-exchange document, for example, retains why dimension-sequential ghost passes were rejected in favor of explicit corner and edge messages. A fresh session recovers project context by reading the overview and the documents of the modules it will touch, which substitutes for the conversational memory the agent lacks.

The session journal under `dev/log/` forms the only append-only component of the system. Every other file evolves toward the current state of the code; the journal instead accumulates one entry per working session and never rewrites the past. It preserves the prompts, interventions, and lessons of sessions whose conclusions the evolving documents have long since absorbed, much as the git history preserves superseded code. Section 4.3 describes how these entries are written and enforced.

4.2. *Task Decomposition and Session Workflow*

The document system controls which project information enters a session; task decomposition controls how much additional context the session generates while work proceeds. Even when a model offers a nominal context window of order 10^6 tokens, retrieval and reasoning can deteriorate well before that limit as relevant information becomes buried in a long context (Liu et al. 2024). In our experience, sessions become unreliable beyond roughly 2×10^5 tokens. Moreover, a long session retains abandoned approaches and debugging detours, which can continue to influence the model's later reasoning. We therefore scope each development task to finish comfortably within a single session.

To reserve a session's limited context for one kind of work, we divide the development of a module into two sessions, one for design and one for implementation. The design session runs as an interactive discussion in which no code is written. The human and the agent iterate on interfaces, memory layout, and the coupling to existing modules, weighing alternatives against the constraints already recorded in the file system. The session ends by writing the module's design document (Section 4.1), which fixes the decisions at a level of detail an implementation can follow. One rule governs the scoping: a task that would force a design decision midway through implementation is too large and is split.

Implementation then starts in a fresh session, so the dead ends of the design debate do not occupy the context. The session loads `AGENTS.md`, the rulebooks matching the files it will touch, and the design document. It opens in a planning mode: the agent lays out its intended changes at the file level, and the human approves the plan before any edit. During implementation the design document acts as the con-

tract, and the agent must surface any deviation from it rather than improvise silently. The interactive REPL that serves human prototyping (Section 3.4) also lets the agent execute and check code incrementally as it works. Before presenting its diff, the agent runs its own gates: the full test suite on the CPU backend, the doctests of new docstrings, and a scan of the diff against the rulebooks.

To catch what an implementation session cannot see in its own output, we review the diff in a new session, or with an agent built on a different model, against the design document and the rulebooks. The bounded documents make this cross-check cheap, because the reviewer needs the contract, not the conversation that produced the code. Tests written during the implementation session validate the physics against analytical or reference solutions where they exist, drawing on the problems of Section 5. The final judgment stays with the human: an agent can make a test pass, but only the human decides whether a shock-tube result is physically right.

The division of labor follows from these gates. The human owns architecture, physics validation, the rulebooks, and every commit; the agent owns the implementation of scoped tasks, their tests, and their documentation. One further obligation attaches to the commit itself; the next subsection describes how it keeps the memory of Section 4.1 current.

4.3. *Interactive Review and Pre-Commit Hooks*

To keep the memory of Section 4.1 current and to turn recurring mistakes into rules, we require every code change to carry a record of the session that produced it. A pre-commit hook, versioned in the repository and enabled once per clone, rejects any commit that changes code without a session-journal entry staged in the same commit. The hook acts at the level of git rather than of any harness, so it binds Claude Code, Codex, and the human alike. Every commit therefore pairs a change with the record of how that change was produced, and the journal can never fall behind the code.

Each journal entry follows a fixed template. It names the tool and the exact model version with its reasoning effort, quotes the key prompts of the session, and summarizes what the agent produced. Its central section records the human interventions: what had to be corrected or redirected, and why; a session that needed none records that too. The commit message ends with a structured trailer naming the same model and effort, so agent contributions stay searchable in the git history. Reading the entry before approving the commit gives the human a compressed audit of the session.

Writing the entry also closes the feedback loop, which Figure 3 summarizes. While logging, the agent reviews the recorded interventions and asks which of them generalize. A recurring mistake becomes a proposed amendment to `AGENTS.md` or the matching rulebook; a change of interface or behavior becomes an update to the design document. The update matters most when a session restructures a module, because the restructure would otherwise leave the design document describing code that no longer exists. The human approves each promotion, and it ships in the same commit as the log entry that motivated it. One early entry, for example,

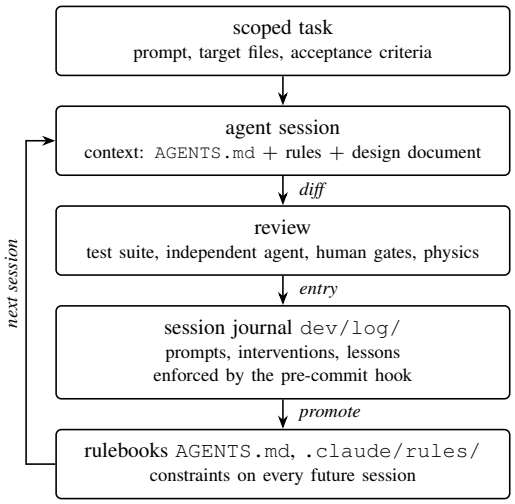

Figure 3. The feedback loop of the development workflow. A scoped task enters an agent session whose context holds the project map, the matching rulebooks, and the design document (Section 4.1). Its diff passes the review gates of Section 4.2. The pre-commit hook of Section 4.3 then forces a session-journal entry, and lessons recorded there are promoted, with human approval, into the rulebooks that constrain every following session.

records the promotion of two such rules. The first forbids temporary files inside the repository; the second requires attribution to name the exact model version and reasoning effort rather than the model family. A later entry records the correction of a recurring mistake. Three successive sessions introduced per-cycle configuration checks inside `run!`; the third intervention was promoted to a rule that restricts all such validation to construction.

The loop gives the workflow the self-correcting character that the third problem of this section asked for. Rules constrain a session; the session yields a journal entry; the entry promotes new rules; the next session starts under the improved constraints. Each pass tightens the rulebooks exactly where recorded failures occurred, so the collaboration hardens as the code grows. The same project memory also supports scientific use of the code. Section 4.4 describes how an agent applies it to simulation setup and execution.

4.4. *Agent-Assisted Simulation Setup and Execution*

Aside from developing `Aether.jl`, the human-agent framework also provides a user-facing way to work with the package, allowing users to configure, test, and launch simulations with an agent. The agent has access to the same project memory that supports development, including the code architecture, public interfaces, tests, and execution environment. Combined with built-in skills, this enables the agent to follow repository-specific procedures for running a problem.

In particular, the `run-problem` skill provides tested procedures for preparing environments, configuring simulations, launching calculations, processing results, and comparing them with verified baselines. The agent therefore does not need to infer the execution workflow from examples alone.

Example scripts and notebooks instead provide scientific configurations that can be adapted to a user's problem.

A user can begin by specifying the physical model, computational domain, initial and boundary conditions, diagnostics, and target hardware. The agent translates these requirements into the `Mesh`, `Simulation`, and `Output` interfaces described above. It can then prepare the required environment and launch the problem on CPUs, GPUs, or distributed MPI processes.

This process naturally supports staged execution. A reduced calculation can first check the simulation configuration and output before the full production run. The same setup can then be transferred to the requested accelerator or distributed configuration. The agent can use the test suite and recorded reference results to identify setup, decomposition, or launch problems before computational resources are committed.

For cluster execution, additional skills encode scheduler commands, rank-to-device binding, MPI configuration, and machine-specific requirements. The agent can use this knowledge to prepare and launch a production job without changing the physical definition of the simulation. These version-controlled procedures preserve operational knowledge together with the code and make it available across user sessions and computing platforms.

As a result, the workflow extends beyond software development to simulation setup, verification, and execution. We regard the workflow, alongside the code it produced, as a result of this project. The numerical tests presented in the following section serve both to verify the solver and to provide reference problems for this broader workflow.

5. NUMERICAL TESTS

To verify that `Aether.jl` produces correct results and to catch regressions during development, we maintain a suite of standard test problems (e.g., Fryxell et al. 2000; Stone et al. 2008, 2020, 2026). When an exact or semi-analytic solution is available, we use it to measure the numerical error directly. For problems without such a solution, we compare the numerical result with a higher-resolution reference calculation that has been checked for convergence, or verify a property that must hold exactly, such as symmetry. The examples presented in this section form a representative subset chosen to exercise the code's main physical models, numerical methods, and mesh geometries. The full regression suite under `test/` extends this coverage with additional tests of accuracy, robustness, boundary conditions, and distributed execution.

All tests presented here can be run through the public interface described in Section 3.4. Jupyter notebooks that reproduce most of the figures are distributed with the code.[3]

5.1. *Sod Shock Tube*

We begin with the shock tube of Sod (1978), the standard first test of a shock-capturing code because its exact solution contains all three hydrodynamic wave families at moderate strength. Before any finer property can be measured, a Godunov scheme must place these nonlinear waves at the correct positions with the correct amplitudes. The initial condition separates two resting states at $x = 0$, with $(\rho, p) = (1, 1)$ on the left and $(0.125, 0.1)$ on the right, and $\gamma = 1.4$. We use 512 cells on $x \in [-0.5, 0.5]$ with PPM reconstruction, the HLLC solver, RK3, and a Courant factor of 0.8.

Figure 4 compares the numerical solution at $t = 0.25$ with the exact one. The initial discontinuity breaks up into a left-moving rarefaction fan, a contact discontinuity, and a right-moving shock. The numerical profiles reproduce the position and strength of all three waves. Both discontinuities remain sharp, spreading over a few cells, and no spurious oscillations develop behind either front. The specific internal energy, the most sensitive of the four quantities shown, deviates only in isolated cells inside the two fronts, the usual footprint of captured discontinuities.

5.2. *Shu-Osher and Brio-Wu Shock Tubes*

We next consider two harder one-dimensional problems, collected in Figure 5, which probe what the Sod tube cannot: the fidelity of the reconstruction behind a shock, and the wave families specific to MHD.

The test of Shu & Osher (1989) sends a Mach 3 shock, initially at $x = -0.8$, into the sinusoidally perturbed density field $\rho = 1 + 0.2\sin(5\pi x)$. The shock compresses the incoming entropy waves into short-wavelength oscillations that numerical diffusion damps, so the test measures how much of this structure a scheme retains at fixed resolution. The left panel of Figure 5 compares two 200-cell runs with the HLLC solver against a reference solution computed with PPM on 8192 cells. Fifth-order WENO-Z reconstruction with RK3 recovers nearly the full amplitude of the post-shock oscillations, while second-order PLM with RK2 visibly clips them (cf. Stone et al. 2020). This difference motivates the higher-order reconstructions of Section 2.4 for flows that carry fine structure through shocks.

The right panel shows the MHD shock tube of Brio & Wu (1988). It extends the Sod initial condition with $\gamma = 2$, a normal field $B_1 = 0.75$, and a transverse field that reverses from $+1$ to -1 across the interface. Its breakup produces wave structures specific to MHD, including a compound wave. Because no exact solution exists, the reference is again a self-converged run on 8192 cells. We plot the transverse velocity v_2, which vanishes initially and therefore responds to every wave in the fan. With 256 cells, PPM reconstruction, the HLLD solver, and RK3, the numerical profile tracks the reference through all fronts and resolves each discontinuity with one to two interior points.

5.3. *Circularly Polarized Alfvén Wave*

Shock tubes confirm wave structure but provide no convergence rate, because discontinuities limit every scheme to first-order accuracy locally. We therefore measure the order of accuracy with the circularly polarized Alfvén wave, the standard smooth test for constrained-transport codes (Tóth

[3] https://github.com/MHDFlows/Aether-Example

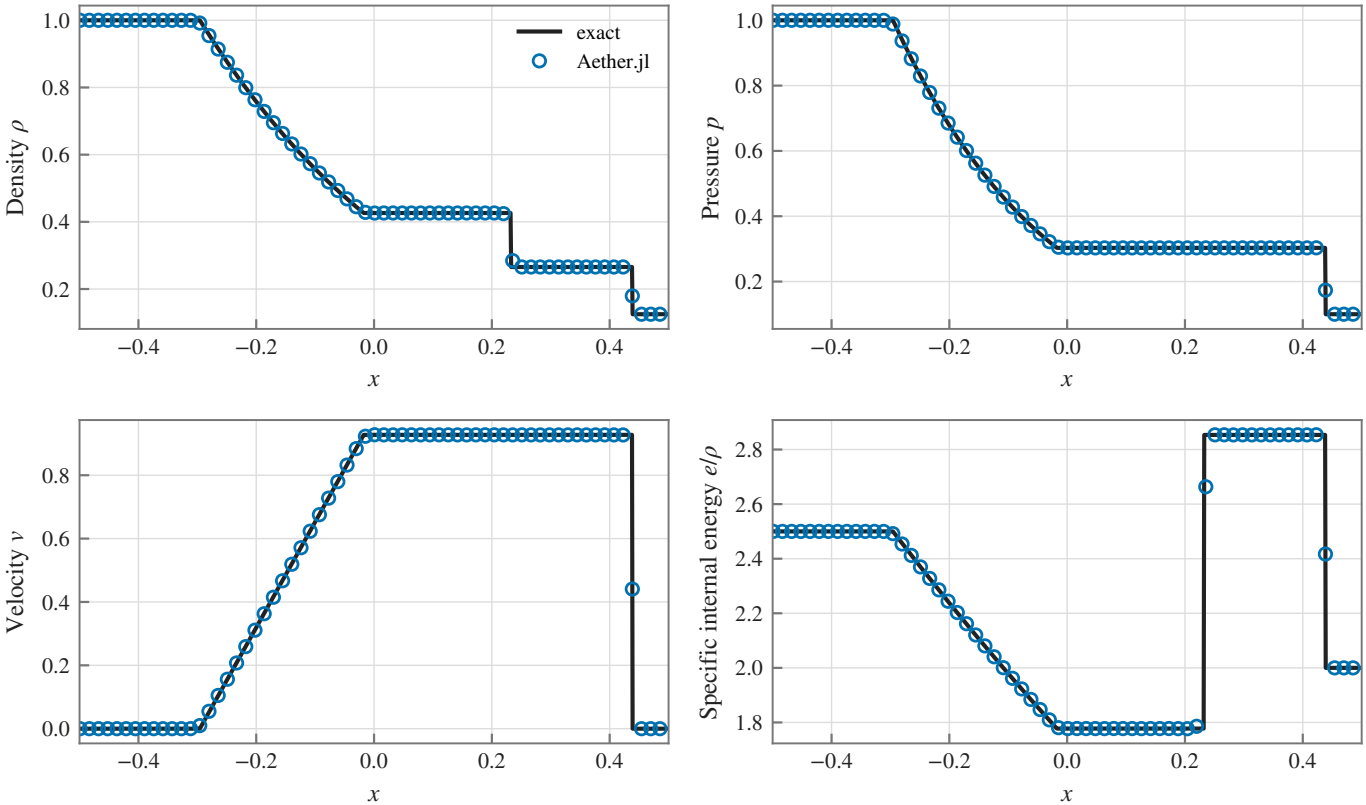

Figure 4. Sod shock tube at $t = 0.25$: density, pressure, velocity, and specific internal energy (every eighth cell shown).

2000; Gardiner & Stone 2008). Because the wave propagates without change of shape as an exact nonlinear solution of ideal MHD, the initial data provide the reference at any later time.

The wave travels along x through a uniform isothermal background with $\rho = 1$, $c_s = 1$, and $B_1 = 1$, so the Alfvén speed is unity. Transverse fields $B_2 = 0.1\sin(2\pi x)$ and $B_3 = 0.1\cos(2\pi x)$, with matching velocities $v_{2,3} = -B_{2,3}$, place one wavelength across the periodic unit cube. We evolve grids of $2N \times N \times N$ cells, with N from 16 to 128, for one crossing time at a Courant factor of 0.3. The L_1 error of B_2 against the initial state then measures the convergence.

Figure 6 shows the errors for two scheme combinations. PPM reconstruction with the LHLLD solver and RK3 converges at a measured order of 2.7 over the finest refinement interval. PLM with HLLE and RK2 converges at order 2.4, with errors 2 to 5 times larger at every resolution. Limiter activity near the wave extrema holds the parabolic scheme below its formal third order, as is common for limited reconstructions on this test.

5.4. *Liska-Wendroff Implosion*

Multidimensional shock reflections expose a property that one-dimensional tests cannot: whether the discrete update treats the two coordinate directions identically. The implosion problem of Liska & Wendroff (2003) makes any violation visible. A low-pressure wedge in the corner of a reflecting box launches a converging shock, and repeated reflections then drive a jet along the diagonal. Because the initial state is mirror-symmetric about that diagonal, any asymmetry in the update deflects or destroys the jet, a failure documented for schemes that break the x-y symmetry.

The domain $[0, 0.3]^2$ initially holds $(\rho, p) = (0.125, 0.14)$ below the line $x + y = 0.15$ and $(1, 1)$ above it, with $\gamma = 1.4$ and reflecting walls. We evolve a 1024^2 grid with PPM, HLLC, and RK3 at a Courant factor of 0.4 to $t = 2.5$, roughly ten acoustic crossings of the box.

Figure 7 shows the resulting density. The jet propagates cleanly along the diagonal, and the fine vortical structures on either side mirror each other. The symmetry holds beyond visual inspection: the density field at $t = 2.5$ equals its transpose in every floating-point bit, so the measured asymmetry is exactly zero. This result confirms that reconstruction, flux evaluation, and the Runge-Kutta combinations evaluate the two directions with identical arithmetic over thousands of cycles.

5.5. *Orszag-Tang Vortex*

The vortex of Orszag & Tang (1979) remains the most widely compared multidimensional MHD test, because its smooth initial data steepen into a reproducible network of interacting shocks and current sheets. The problem already appeared in Section 3.4 as the complete setup script of Figure 2; the runs here use the same script with different resolution and scheme settings. On the periodic unit square, the initial state has $\rho = 25/(36\pi)$, $p =$

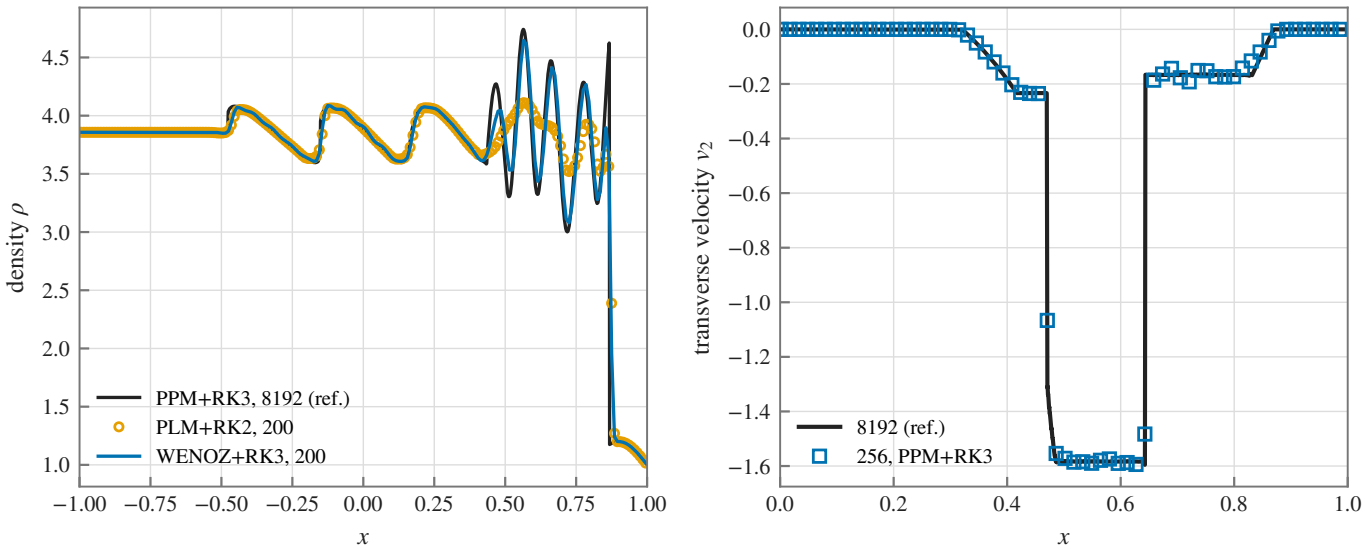

Figure 5. Left: density in the Shu-Osher problem at $t = 0.47$. Right: transverse velocity v_2 in the Brio-Wu MHD shock tube at $t = 0.1$ (every fourth cell shown).

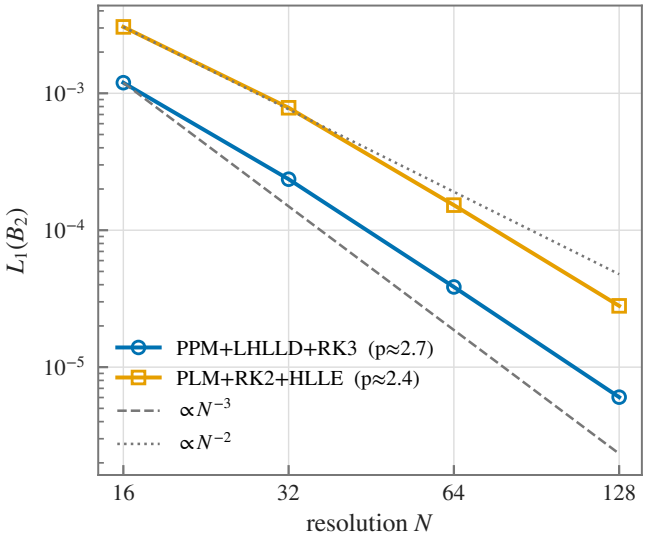

Figure 6. L_1 error of B_2 for the circularly polarized Alfvén wave after one crossing of the periodic domain, as a function of resolution N. The legend quotes the convergence order measured over the finest refinement interval; dashed and dotted guides show slopes of -3 and -2.

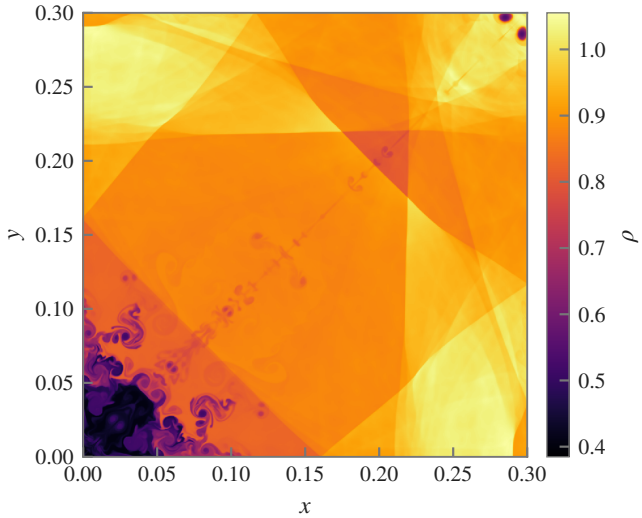

Figure 7. Density in the Liska-Wendroff implosion at $t = 2.5$ on a 1024^2 grid.

$5/(12\pi)$, $\gamma = 5/3$, and velocity $(-\sin 2\pi y, \sin 2\pi x)$. The magnetic field derives from the vector potential $A_3 = B_0\,[\cos(4\pi x)/(4\pi) + \cos(2\pi y)/(2\pi)]$ with $B_0 = 1/\sqrt{4\pi}$, so the field starts divergence-free on the faces. We run resolutions of 256^2 through 2048^2 with PPM5, the LHLLD solver, and RK3 at a Courant factor of 0.4, stopping at $t = 0.5$.

The density map in Figure 8 reproduces the familiar morphology of the test at this time, including the central current sheet, the surrounding shock fronts, and the compressed filaments between them (cf. Stone et al. 2008, 2020). For a quantitative comparison, the right panel cuts the pressure along $y = 0.3125$, a line commonly used in cross-code studies. Away from the sharpest features the four resolutions already coincide, so the inset magnifies $x \in [0.02, 0.14]$, where the narrow spike and dip differ most. The coarsest run smooths both features, and each refinement roughly halves the remaining deviation until the 1024^2 profile lies on the reference. All fronts remain free of oscillations.

5.6. *Sedov-Taylor Blast Wave*

A point explosion into a cold uniform medium follows the self-similar solution of Taylor (1950) and Sedov (1959), which fixes the shock radius and the interior profiles at every time. We run this problem on a spherical-polar mesh, where it exercises the geometric source terms, the exact metric factors, and the polar-axis boundary of Section 2.3. Because

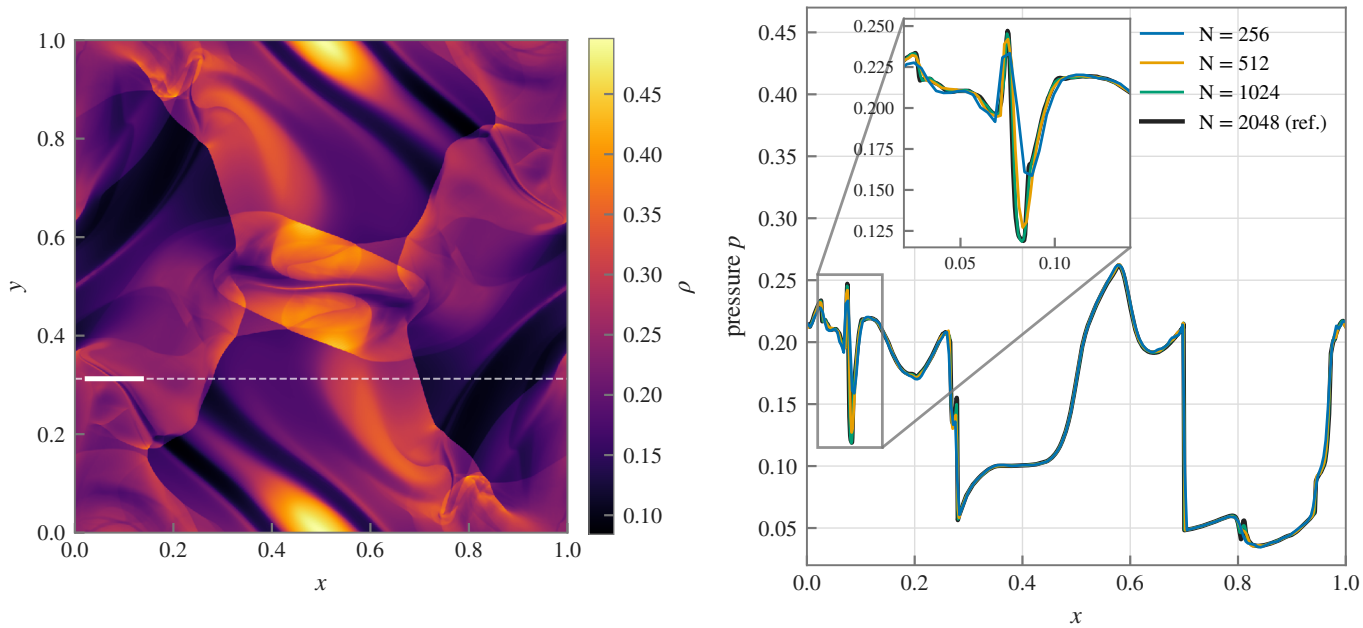

Figure 8. Orszag-Tang vortex at $t = 0.5$. Left: density on the 1024^2 grid; the dashed line marks the cut at $y = 0.3125$, and the solid segment marks the interval magnified in the inset. Right: pressure along the cut for resolutions of 256^2 to 2048^2; the inset magnifies the marked interval.

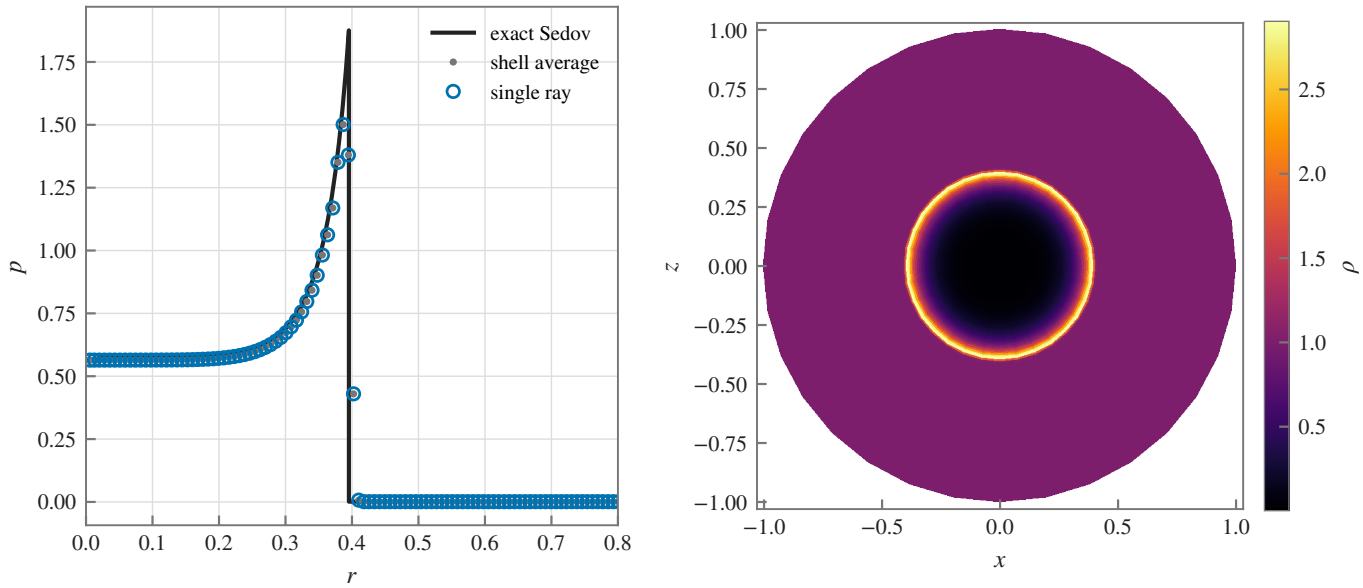

Figure 9. Sedov-Taylor blast wave at $t = 0.1$ on the spherical-polar mesh. Left: pressure against radius; gray points give the shell averages, open circles a single (θ, ϕ) ray, and the black line the self-similar solution for the deposited energy. Right: density in the meridional plane, mapped to Cartesian coordinates; the grid axis runs vertically through the panel.

the exact flow is spherically symmetric, any angular structure that develops measures the numerical error directly.

The mesh covers the full sphere $r \in (0, 1)$ with $(N_r, N_\theta, N_\phi) = (128, 16, 32)$ cells. The ambient gas has $\rho = 1$ and $p = 10^{-3}$ with $\gamma = 5/3$, and the blast deposits internal energy uniformly inside $r_0 = 0.02$. Because only the two innermost radial shells have centroids inside r_0, the discrete initial condition holds $E = 0.477$ rather than the nominal unit energy; the analytic profile uses this deposited value. We combine positivity-preserving WENO-Z reconstruction, HLLC, and RK3 at a Courant factor of 0.3. The boundaries pair a reflecting inner radius with outflow at $r = 1$ and the polar condition at the axis, and the run stops at $t = 0.1$.

The left panel of Figure 9 compares the pressure with the self-similar solution. Solid-angle-weighted shell averages over all 512 angular zones coincide with a single sampled ray to the width of the markers. At each radius, the pressure in every angular zone matches the shell mean to a rela-

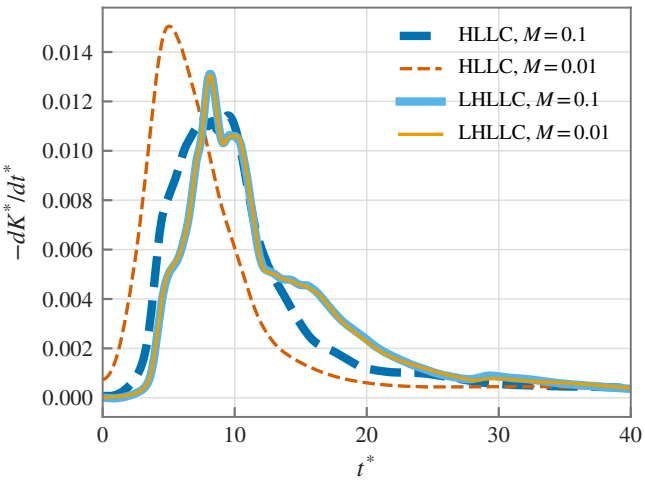

Figure 10. Kinetic-energy dissipation rate of the three-dimensional Taylor-Green vortex in scaled units, for HLLC (dashed, dark tones) and LHLLC (solid, light tones) at maximum initial Mach numbers of 0.1 (thick blue) and 0.01 (thin orange). The thin LHLLC curve lies inside the thick one.

tive deviation below 3×10^{-13}, so the blast remains spherically symmetric to near machine precision. The shock front sits at the predicted radius, while the finite radial resolution smooths the pressure spike behind it and lowers the sampled peak. The meridional density slice in the right panel shows the same result geometrically: a thin, round shell that crosses the grid axis at the top and bottom of the panel without distortion.

5.7. *Taylor-Green Vortex at Low Mach Numbers*

The tests above exercise the solvers at Mach numbers of order unity or above, yet much astrophysical dynamics is subsonic. Turbulence in the solar wind and the magnetic reconnection embedded in it evolve at small fractions of the sound speed (Bruno & Carbone 2013; Zweibel & Yamada 2009). In planet-forming disks, the instabilities that concentrate solids into planetesimals grow from velocities of a few percent of the sound speed (Youdin & Goodman 2005). Standard upwind solvers lose accuracy in this regime: their pressure dissipation stays proportional to the sound speed, while the physical pressure fluctuations decrease as the square of the Mach number (Guillard & Viozat 1999). These solvers therefore damp subsonic motions that the grid resolves. To verify that LHLLC removes this failure, we measure the numerical dissipation of a decaying vortex at two Mach numbers, following Barsukow et al. (2017).

The vortex of Taylor & Green (1937) starts as a single large-scale mode in a periodic cube and decays into progressively smaller vortices. Because the setup carries no explicit viscosity, the decay of the mean kinetic energy K measures the numerical dissipation alone. The initial state has uniform density, velocity $\mathbf{v} = V_0\,(\sin x \cos y \cos z,\, -\cos x \sin y \cos z,\, 0)$, and a uniform pressure that sets the maximum Mach number $M = V_0/c_{\rm s}$, plus the pressure perturbation of order ρV_0^2 that accompanies the vortex. When time is scaled by the vortex turnover and kinetic energy by V_0^2, runs at different Mach numbers approach the same incompressible limit, so the scaled dissipation rate should not depend on M. We run $M = 0.1$ and $M = 0.01$ on a 128^3 grid with PLM reconstruction and RK2, once with HLLC and once with LHLLC.

Figure 10 compares the four runs. The two LHLLC curves coincide, agreeing to within 1% of the peak dissipation rate over the whole run, so the numerical dissipation is independent of the Mach number, as required. The HLLC curves instead separate: at $M = 0.01$ the peak dissipation rate is 32% higher than at $M = 0.1$ and occurs at half the scaled time. This contrast reproduces the behavior of the standard and low-Mach Roe fluxes in Figure 7 of that study. We therefore recommend the low-dissipation solvers for subsonic applications.

5.8. *Multifluid Dust*

The remaining tests validate the dust module, which couples an arbitrary number of pressureless fluids to the gas through stiff drag (Section 2.2). Its solver relies on algorithms the fluid tests above do not exercise: the pressureless Riemann solver, the closed-form implicit drag stage, and the `IMEX2P` integrator of Section 2.6. We adopt three one-dimensional problems from the benchmark set of Benítez-Llambay et al. (2019), which probe the relevant regimes in turn. A linear wave tests the accuracy of the coupled oscillation, a nonlinear steady shock tests several species with distinct coupling strengths, and a uniform relaxation problem tests the drift equilibrium under external forcing. All three problems run isothermal with `IMEX2P`.

5.8.1. *Damped Dusty Sound Wave*

Sound waves in a dusty medium damp and disperse, because drag exchanges momentum between the phases on each stopping time. For small amplitudes the coupled equations linearize exactly, so the full time history of every fluid follows from a single complex eigenmode. This property makes the problem a sharp accuracy test for the coupled gas-dust update.

We use $c_{\rm s} = 1$, $\rho_{\rm g} = 1$, and four dust species with dust-to-gas ratios $\varepsilon = (0.100, 0.233, 0.367, 0.500)$ and stopping times spaced logarithmically from 0.1 to 1. Linearizing the ten coupled equations at wavenumber $k = 2\pi$ and selecting the least-damped oscillatory mode gives the eigenvalue $\lambda = -0.912 \pm 5.494\,i$. We initialize all ten fields from the corresponding eigenvector at relative amplitude 10^{-4} on 128 cells. The run then follows the wave for two time units, about 1.7 oscillation periods and 1.8 damping times.

Figure 11 tracks the normalized density perturbation of every fluid at a fixed cell. The gas and all four dust species follow the analytic mode in phase and amplitude through the full decay. This agreement verifies the drag coupling in both directions together with the pressureless advection of each species.

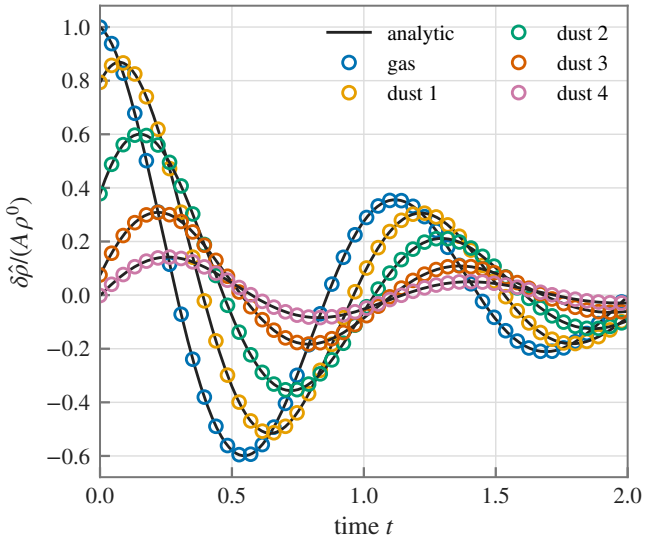

Figure 11. Damped dusty sound wave with four dust species: normalized density perturbations at a fixed cell. Markers subsample the numerical record; black lines show the analytic eigenmode evolution.

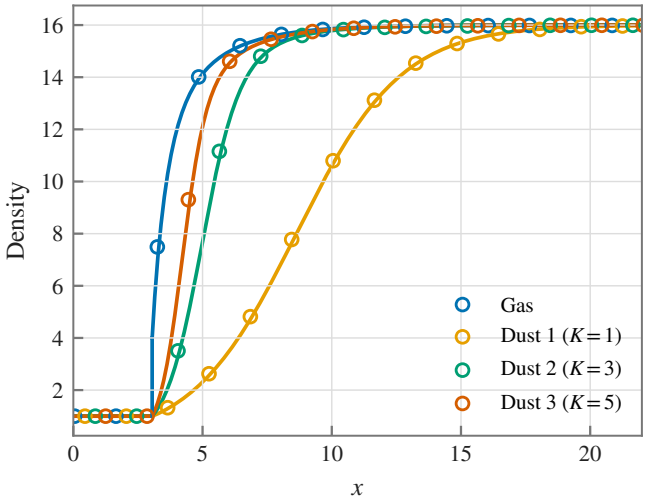

Figure 12. Steady isothermal dusty shock with three dust species. Open markers show the stationary `Aether.jl` profiles; solid lines the semi-analytic reference.

5.8.2. *Steady Dusty Shock*

Behind a shock in a dusty medium, each species returns to the gas velocity over its own drag length, so a steady shock develops a layered relaxation structure that tests every coupling strength at once. The stationary equations reduce to ordinary differential equations in x, and their numerical integration provides a semi-analytic reference (Benítez-Llambay et al. 2019).

We drive an isothermal Mach 2 flow, with $v = 2$ and $c_s = 1$, through a standing shock while carrying three dust species, each at the gas density. The drag uses constant coefficients $K = 1$, 3, and 5, corresponding to stopping times $t_{s,k} = \rho_k/K_k$. The dust triples the inertia of the mixture, so the effective sound speed of the fully coupled fluid halves. The far-downstream compression therefore reaches the square of the effective Mach number, a factor of 16. We initialize the two equilibrium states as a discontinuity on a domain of length 40 with 400 cells and relax the flow to a stationary profile by $t = 500$.

Figure 12 overlays the numerical densities on the integrated reference. The gas jumps at the front and then compresses smoothly as the dust catches up. Each species relaxes over a length set by its drag coefficient, and all four profiles follow the reference through the entire layer.

5.8.3. *Drag Relaxation Under External Forcing*

Section 2.6 integrated drag inside the stages rather than operator splitting it, because splitting fails to reach the correct drift equilibrium when external forces act (Krapp et al. 2024). Our final test checks that equilibrium directly. A spatially uniform mixture carries gas of density 1 and two dust species of density 0.1 each, with stopping times 1 and $4/3$, starting from velocities 2, 0.1, and -0.5. A constant acceleration $g = 1$ pushes the gas alone, so the mixture cannot settle into a comoving state. The exact solution of the linear system instead approaches rigid acceleration at $\bar{a} = g\rho_g/\rho_{tot} \approx 0.83$, with each species trailing the gas by the terminal drift $v_g - v_{d,k} = \bar{a}\, t_{s,k}$.

Figure 13 shows both views of the relaxation. The velocity differences decay onto the predicted terminal drifts, and the three velocities settle onto parallel linear growth at $\bar{a}$, matching the matrix-exponential solution throughout. The automated suite repeats this problem in the stiff regime, with the timestep exceeding the shortest stopping time by an order of magnitude, and recovers the same drift equilibrium to better than one part in 10^8. This result confirms the L-stability of the implicit stages in a regime the resolved runs shown here cannot reach.

6. PERFORMANCE

Section 1 asked whether a dynamic language can deliver the performance and scalability expected of a production astrophysics code on modern GPU hardware. In this section, we test whether that goal has been achieved, presenting the results of single-device performance and weak scaling tests on data-center, consumer, and exascale hardware.

Every benchmark below runs in double precision. Because Julia compiles specialized kernels on first execution, each measurement begins after a warm-up phase that absorbs this one-time cost and covers the following 2000 cycles.

6.1. *Single-Device Performance*

To test whether kernels compiled from one Julia source remain competitive on hardware from different vendors, we run the same benchmark, unchanged, on three devices. The set comprises an NVIDIA A100 (40 GB) in the Perlmutter system at NERSC; one Graphics Compute Die (GCD) of an AMD MI250X in Frontier, a test system at the Oak Ridge

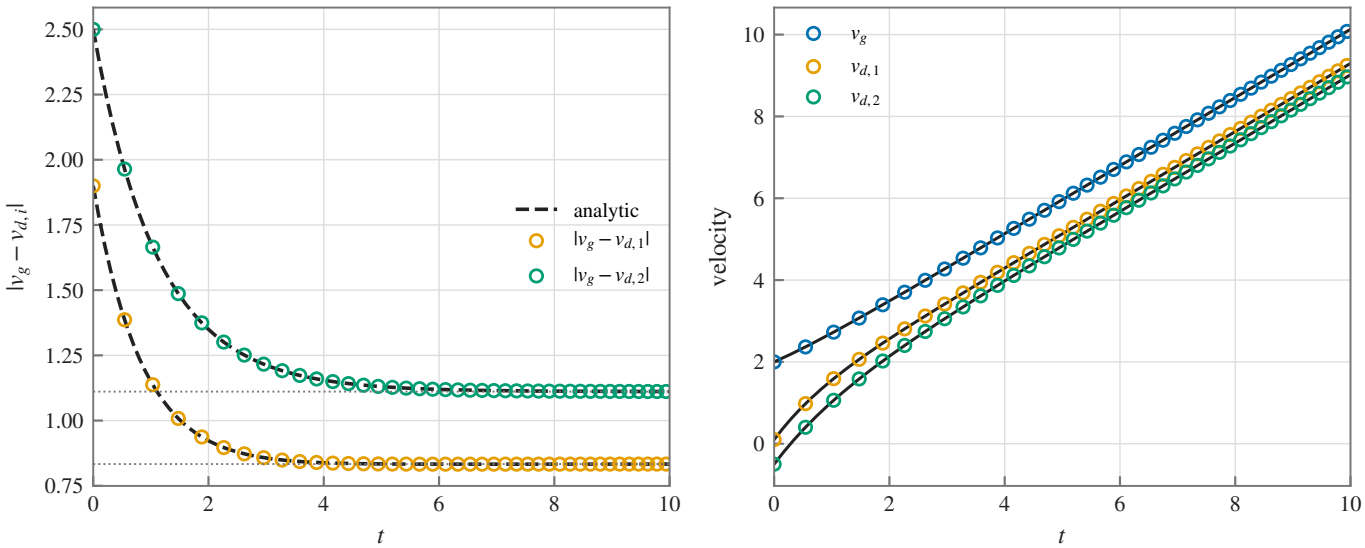

Figure 13. Drag relaxation under a constant acceleration applied to the gas alone. Left: gas-dust velocity differences; dashed lines show the exact solution, dotted lines the terminal drifts. Right: the three velocities against time.

Table 2. Single-device throughput on the three-dimensional linear-wave benchmark, in Mzcps.

Device	Hydro	MHD
NVIDIA A100 (40 GB)	709	300
AMD MI250X (one GCD)	478	250
NVIDIA RTX 4090 (24 GB)	215	122

Leadership Computing Facility (OLCF) with the same nodes as the exascale system Frontier; and a consumer NVIDIA RTX 4090 (24 GB). The software stack exposes each GCD of an MI250X as an independent device, so per-GCD rates are the natural unit on this hardware.

For a direct comparison between the static and dynamic language, we adopt the single-device benchmark of AthenaK (Stone et al. 2026). The benchmark advances a three-dimensional linear wave across a periodic uniform grid; the smooth solution keeps the work per cell uniform, so the timing reflects the sustained cost of the full update loop. Both the hydrodynamic and the MHD solver advance the wave using PLM reconstruction, the HLLE Riemann solver, and the `RK2` integrator. On the A100 and the MI250X the grid holds $512 \times 512 \times 256$ cells, tiled into 128^3 blocks; the smaller memory of the RTX 4090 restricts its grid to 256^3 cells at the same block size.

Table 2 lists the measured throughput in millions of zone-cycles per device-second (Mzcps); the metric counts each cell once per cycle regardless of the stage count of the integrator. The A100 sustains 709 Mzcps in hydrodynamics and 300 Mzcps in MHD, and a single MI250X GCD reaches 478 and 250 Mzcps. Across the three devices the MHD update costs 1.8 to 2.4 times the hydrodynamic update. The ratio reflects the additional induction equation, the constrained-transport update, and the more expensive Riemann problem.

These rates place `Aether.jl` in the performance class of contemporary compiled-language GPU codes. Running the same combination of PLM, HLLE, and `RK2` on the same problem in double precision, AthenaK reports 614 and 298 Mzcps for hydrodynamics and MHD on an A100, and 405 and 190 Mzcps on the closely related AMD MI250. The rates in Table 2 match or exceed these values on both architectures. This comparison suggests that dynamic Julia code runs comparably to statically compiled C++ code, and possibly slightly faster.

We include the consumer RTX 4090 to test performance on hardware outside the data center. Consumer GPUs execute double-precision arithmetic at $1/64$ of their single-precision rate, so a large penalty might be expected. However, the measured rates of 215 and 122 Mzcps instead fall only a factor of 2.5 to 3.3 below the A100. This suggests that it is the memory bandwidth, not arithmetic, limits most kernels of a finite-volume update (Grete et al. 2021), and the bandwidth gap between the two cards is far smaller than their arithmetic gap. A personal computer therefore supports serious development and moderate production runs, which extends the single-language workflow to hardware a student may already own.

6.2. *Weak Scaling*

To test parallel scaling at the scale of production simulations, we perform a weak scaling test on the Frontier system at OLCF. Each Frontier node carries four MI250X accelerators, hence eight GCDs, and one MPI rank drives each GCD. The workload per device stays fixed as the machine grows, so any increase in the time per cycle measures communication overhead and load imbalance. The benchmark evolves driven isothermal MHD turbulence under stochastic forcing, so the timed loop includes the forcing kernels, the timestep reduction, and every communication step. Each GCD carries a fixed load of 1.68×10^7 cells, and the node count grows

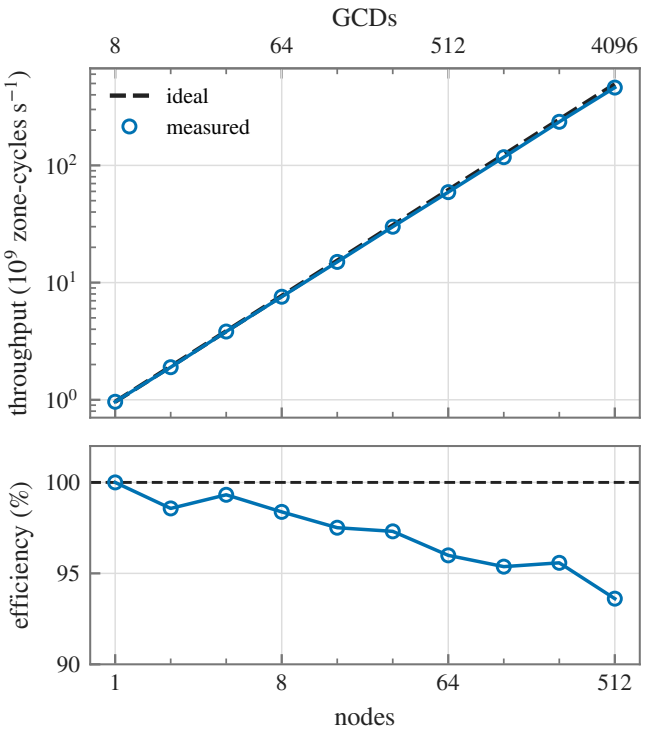

Figure 14. Weak scaling of the driven-turbulence benchmark on Frontier. Top: aggregate throughput against node count, with the dashed line marking ideal scaling from the single-node rate; the upper axis counts GCDs. Bottom: parallel efficiency relative to one node.

in powers of two from 1 to 512, so the largest run updates 6.9×10^{10} cells on 4096 GCDs.

Figure 14 shows the aggregate throughput and the parallel efficiency, the single-node time per cycle divided by its value at each node count. Throughput rises from 9.6×10^8 zone-cycles per second on one node to 4.6×10^{11} on 512 nodes. Efficiency stays at or above 93.6% throughout. A solver written in Julia therefore sustains competitive per-device throughput and near-ideal weak scaling in large-scale runs.

7. EXAMPLE APPLICATIONS

The previous sections validate individual algorithms and measure performance on controlled workloads. Here we show how the components of `Aether.jl` work together in full production simulations. The first is a 2048^3 simulation of driven multiphase turbulence in the interstellar medium; the second follows the vertical shear instability in a protoplanetary disk containing 48 dust species.

7.1. *Multiphase Interstellar Turbulence*

Compressible turbulence has long driven the largest uniform-grid calculations in computational fluid dynamics. Studies of the universality of the cascade reached $10{,}048^3$, resolving the sonic scale (Federrath et al. 2021), and the magnetized counterpart of that measurement runs at $10{,}080^3$ (Beattie et al. 2025).

Behind these isothermal idealizations, the simulated gas is usually interpreted as the cold, dense component of the turbulent interstellar medium, where rapid cooling keeps the gas isothermal. A more comprehensive model, however, must include its multiphase nature. Heating and cooling maintain a warm phase near 10^4 K and a cold phase near 10^2 K in rough pressure balance (Wolfire et al. 1995, 2003; Heiles & Troland 2005), while turbulence continually drives gas across the thermally unstable branch between them (Koyama & Inutsuka 2002). The rapid heating and cooling change the properties of the turbulence itself: the density and pressure statistics, and the energy spectra may depart from the isothermal case (Kritsuk et al. 2017). Recent high resolution multiphase simulations have been used to study the plasmoid instability (Fielding et al. 2023), the polarized Galactic dust foreground (Ho et al. 2025; Kritsuk et al. 2026), and phase-dependent magnetic coherence (Butsky et al. 2026).

In such simulations, the warm phase remains transonic while the cold phase, whose sound speed is ten times lower, reaches $\mathcal{M}_\mathrm{s} \gtrsim 10$ across shocks connecting densities below $1\ \mathrm{cm}^{-3}$ to above $100\ \mathrm{cm}^{-3}$. There the internal energy is only a percent of the total (Equation 5), reconstruction overshoots could drive the pressure negative, and the pressure floor overwrites the temperature. As a result, the numerical scheme no longer evolves the thermodynamics of the gas correctly. The dual-energy formalism solves this problem: it keeps the pressure positive and accurate even when the internal energy is a small fraction of the total.

Using this formulation, we evolve a 200 pc periodic box on a 2048^3-cell grid with PPM reconstruction, the LHLLD solver, and `RK2`, assuming $\gamma = 5/3$. Implicit cooling and heating act with fully solenoidal driving at $1 \le kL/2\pi \le 2$ on an initially uniform medium, $n_\mathrm{H} = 1\ \mathrm{cm}^{-3}$, threaded by a uniform field. Driving power and field strength put the saturated warm phase near $\mathcal{M}_\mathrm{s} \approx 1.2$ and $\mathcal{M}_\mathrm{A} \approx 2$.

The simulation was run on 256 Frontier nodes for two warm-phase sound-crossing times and completed in about four hours of wall clock.

Figure 15 shows a slice of the resulting density and temperature fields. The dual-energy closure holds both phases at their equilibrium temperatures, from the volume-filling warm gas down to cold knots a few cells across. Their boundaries stay sharp at the grid scale. Between them, gas crossing the unstable range has no equilibrium to return to, and the closure alone preserves its thermal history. A full analysis of the phase structure and of the synthetic polarization statistics will be presented elsewhere.

7.2. *Vertical Shear Instability with 48 Dust Species*

In protoplanetary disks, the dynamics of dust depends not only on its total mass but on how that mass is distributed over grain size. Grains of different sizes settle, drift, and are stirred at different rates. The same distribution sets the opacity, and with it the thermal structure of the disk (Testi et al. 2014; Birnstiel et al. 2016).

Dust-driven instabilities respond to the full distribution rather than to a mean grain size: growth rates of the streaming

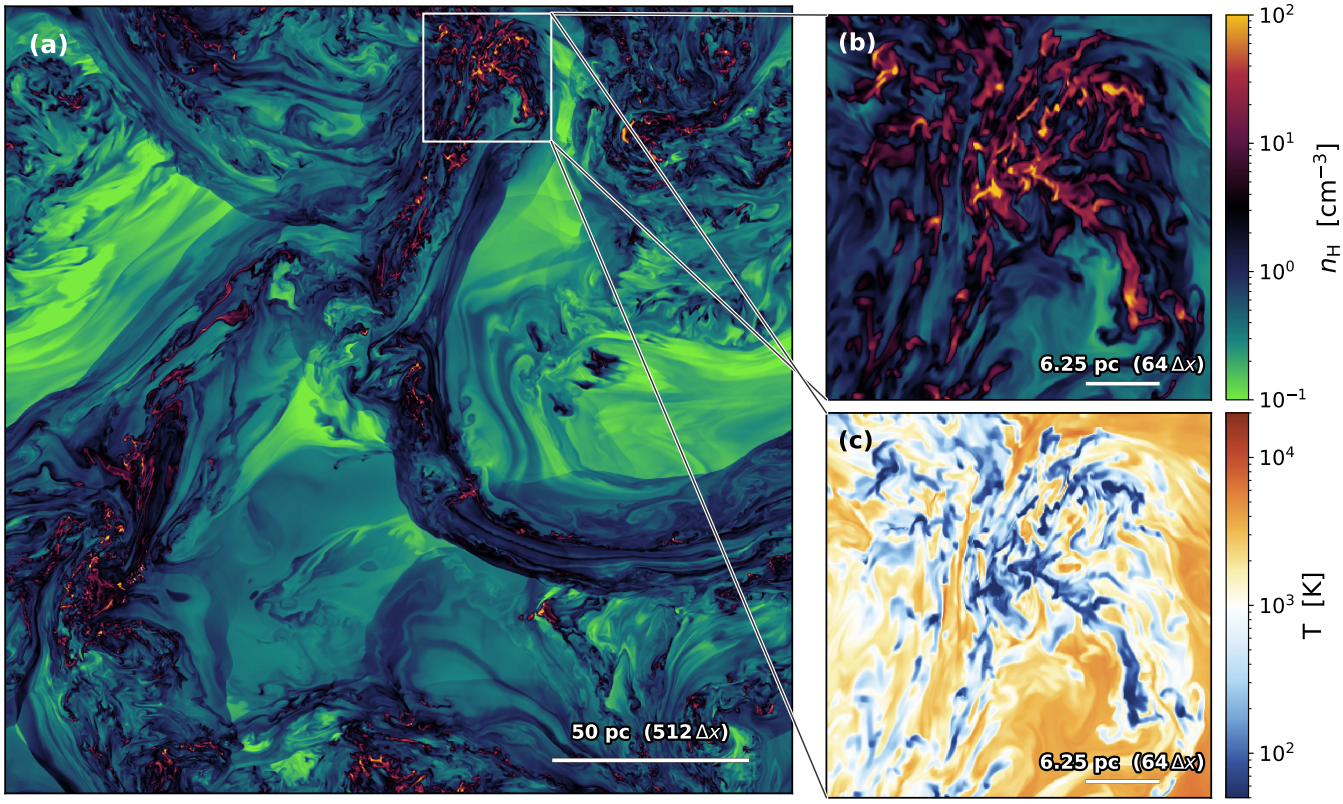

Figure 15. Slice of the hydrogen number density in the saturated state of the multiphase turbulence run (a). Zoomed-in views of the boxed region show the cold dense filaments and the surrounding warm gas in number density (b) and temperature (c). Scale bars give lengths in parsecs and in grid cells.

instability change qualitatively once a size spectrum replaces a single species (Krapp et al. 2019; Schaffer et al. 2018; Zhu & Yang 2021; Yang & Zhu 2021; McNally et al. 2021; Rucska & Wadsley 2023). The vertical shear instability (VSI; Nelson et al. 2013; Stoll & Kley 2014) stirs grains at rates that depend on their size (Stoll & Kley 2016; Flock et al. 2017, 2020), while the dust in turn alters the cooling rate on which the instability depends (Dullemond et al. 2022; Pfeil et al. 2023; Fukuhara & Okuzumi 2024).

Grains also coagulate and fragment on timescales comparable to settling and drift. Evaluating the collision kernel in every cell is expensive in CPU time, so such modeling has stayed largely one-dimensional (Brauer et al. 2008; Birnstiel et al. 2010; Estrada et al. 2016; Stammler & Birnstiel 2022), and couplings to multidimensional hydrodynamics remain rare (Drażkowska et al. 2019; Laune et al. 2020; Li et al. 2020; Ho et al. 2024). Here we demonstrate the transport side of that coupling at production scale: the dust module of `Aether.jl` evolves the full grain size distribution through a disk instability. In the future, on-the-fly coagulation could then be added as a user-defined source term within the source framework of `Aether.jl`, compatible with current methods (Birnstiel et al. 2010; Lombart & Laibe 2021; Lombart et al. 2024; Yang et al. 2026).

We simulate the VSI with 48 dust species, in the axisymmetric equilibrium disk of Nelson et al. (2013) around a $GM = 1$ point mass: aspect ratio $h = 0.05$, midplane density $\propto R^{-2}$, and $c_s^2 = h^2\, GM/R$ on cylindrical radius R. Gravity enters as a user-defined source term. The VSI requires rapid cooling toward a locally isothermal state (Lin & Youdin 2015). A per-stage hook therefore resets the internal energy of the $\gamma = 7/5$ gas to this profile, with drag heating disabled.

The species sample grain radii log-uniformly from 10^{-6} to 1 cm, with mass weights following the Mathis et al. (1977) distribution $n(a) \propto a^{-3.5}$ at total dust-to-gas ratio $Z = 0.01$. For $r_0 = 50$ au around a solar mass, with the minimum-mass solar nebula surface density $\Sigma_g = 4.8\,\mathrm{g\,cm^{-2}}$ (Hayashi 1981) and material density $1.25\,\mathrm{g\,cm^{-3}}$, Epstein drag gives midplane Stokes numbers from 4.1×10^{-7} to 0.41.

The axisymmetric spherical-polar mesh spans $r \in [0.5, 2]\, r_0$ and $\theta = \pi/2 \pm 4h$ with 3072×1024 uniform cells, 102 radial and 128 meridional per scale height. This exceeds published convergence requirements for the instability (Flores-Rivera et al. 2020; Manger et al. 2020). We combine PPM with HLLC for the gas, the pressureless HLL flux for the dust, and `IMEX2P` at a Courant factor of 0.4.

The dust starts from the drift equilibrium of Nakagawa et al. (1986), generalized to many species (Benítez-Llambay et al. 2019), with each species settled to a scale height $h_d = h\sqrt{\delta_0/(\delta_0 + \mathrm{St})}$ at $\delta_0 = 10^{-3}$ (Dubrulle et al. 1995; Youdin & Lithwick 2007) and floored at three cells. A ran-

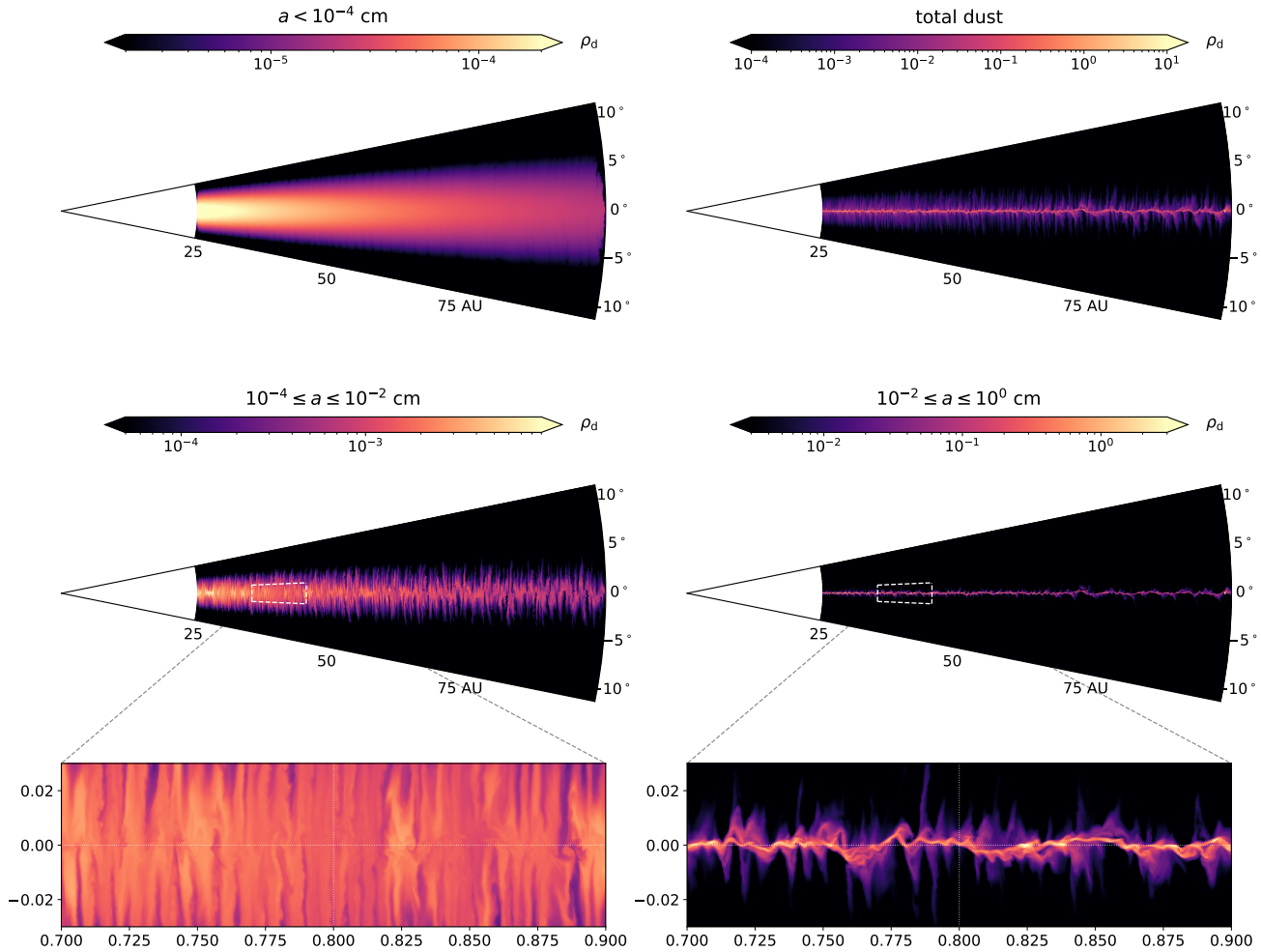

Figure 16. Dust density in the 48-species VSI run after saturation of the instability. Top: meridional maps of the dust density, in code units, summed over three grain-size bins ($a < 10^{-4}$ cm, $10^{-4} \le a \le 10^{-2}$ cm, $10^{-2} \le a \le 1$ cm) and over all species. The wedges cover the full domain, 25 to 100 au in radius and $\pm 11.5°$ about the midplane. Bottom: magnifications of the boxed regions of the two larger-size bins, spanning $r \in [0.70, 0.90]\, r_0$ (35 to 45 au) and $|z| \le 0.03\, r_0$ (± 1.5 au).

dom meridional velocity perturbation of $10^{-3}\, c_s$ seeds the instability. Dirichlet boundaries hold all four faces at the initial equilibrium, so the outer face resupplies inward-drifting dust and the disk reaches a drift-through steady state. The run advances 125 orbits at r_0, about 44 kyr in 1.54×10^6 cycles, on two Frontier nodes in twelve hours of wall clock. With 49 fluids per cell it sustains 1.18×10^8 zone-cycles per second, or 3.6×10^8 per-species cell updates per GCD-second, on par with the single-fluid rates of Table 2.

Figure 16 shows the resulting dust density in three size bins and in total. The smallest grains ($\mathrm{St} \lesssim 4 \times 10^{-5}$) spread through the full domain and trace the gas. Intermediate sizes follow the corrugated columns of the VSI body modes, resolved across dozens of cells in the left zoom. The largest grains settle into a thin midplane layer that the corrugation bends and locally disrupts (right zoom). Edge-on disks show the same stratification of well-mixed small grains around a thin pebble layer. A quantitative analysis of the size-dependent scale heights and drift-through fluxes will follow in a dedicated paper.

8. DISCUSSION AND SUMMARY

In this paper, we demonstrate how to build a high-performance MHD solver in a dynamic language, and describe the workflow and framework for developing a complicated multifluid code through an interactive workflow with coding agents. Whether the workflow sustains the code through years of maintenance remains open and interesting questions.

`Aether.jl` itself implements finite-volume compressible MHD with multifluid dust in Julia. The code is verified against standard test problems, matches the throughput of contemporary C++ GPU codes, and holds above 93% parallel efficiency on 4096 GCDs of Frontier. Two production applications showcase ran at 2048^3 cells and a 2D run with 48 dust species.

`Aether.jl` currently targets applications in astrophysical turbulence and its coupling to multiphysics, from the multiphase interstellar medium to protoplanetary disks. Beyond these applications, Julia's single-language design gives the solver access to a wider scientific ecosystem. The stiff integrators of `DifferentialEquations.jl` and their GPU ensemble variants (Rackauckas & Nie 2017; Utkarsh et al. 2024) could evolve astrochemical networks in every cell (e.g., Grassi et al. 2014). Large networks may make direct integration too expensive. A neural surrogate built with `Lux.jl` (Pal 2023) could approximate the local solve and be evaluated on CPU or GPU arrays within the same Julia program. Fluid solvers increasingly incorporate such models (Kochkov et al. 2021; Li et al. 2021; Lu et al. 2021), and stiff astrochemistry has already been emulated with autoencoders and neural operators (Grassi et al. 2022; Branca & Pallottini 2024). On-the-fly grain coagulation poses a similar cell-local problem and could use either strategy.

These extensions suggest a broader model for simulation software. A Julia simulation can be assembled from interoperable scientific libraries instead of growing as a closed executable. The fluid solver, local physics modules, analysis routines, and learned components can share data structures within one program. Researchers can develop a new physical model interactively, couple it directly to the time-stepping loop, deploy it on CPUs or GPUs, and analyze the results without rewriting the model in another language. This structure brings prototyping, production simulation, and analysis into a unified Julia workflow. The results presented here show that such integration can retain the performance and scalability required for production astrophysics.

ACKNOWLEDGMENTS

The author thanks Alexei G. Kritsuk for insightful discussions and constructive comments on the manuscript. The author also thanks the organizers of the 2026 LANL Julia for Science Training Workshop for the valuable technical insights gained during the workshop. This research used resources of the National Energy Research Scientific Computing Center, a DOE Office of Science User Facility supported by the Office of Science of the U.S. Department of Energy under Contract No. DE-AC02-05CH11231, using NERSC awards ASCR-ERCAP0036667 and FES-ERCAP0036102. Additional computational and storage resources were provided through the Director's Discretion allocation at Oak Ridge National Laboratory (ORNL), award AST193. This research was supported by grants 216179 from the Simons Foundation and NSF PHY-2309135 to the Kavli Institute for Theoretical Physics (KITP).

Software: `Aether.jl`, Julia (Bezanson et al. 2017), KernelAbstractions.jl (Churavy et al. 2021), CUDA.jl (Besard et al. 2019), AMDGPU.jl (Samaroo et al. 2026), MPI.jl (Byrne et al. 2021), ADIOS2 (Godoy et al. 2020), ADIOS2.jl, Matplotlib

REFERENCES

Ascher, U. M., Ruuth, S. J., & Spiteri, R. J. 1997, Applied Numerical Mathematics, 25, 151, doi: 10.1016/S0168-9274(97)00056-1

Austin, J., Odena, A., Nye, M., et al. 2021, arXiv e-prints, doi: 10.48550/arXiv.2108.07732

Balsara, D. S., Garain, S., & Shu, C.-W. 2016, Journal of Computational Physics, 326, 780, doi: 10.1016/j.jcp.2016.09.009

Barsukow, W., Edelmann, P. V. F., Klingenberg, C., Miczek, F., & Röpke, F. K. 2017, Journal of Scientific Computing, 72, 623, doi: 10.1007/s10915-017-0372-4

Batten, P., Clarke, N., Lambert, C., & Causon, D. M. 1997, SIAM Journal on Scientific Computing, 18, 1553, doi: 10.1137/S1064827593260140

Beattie, J. R., Federrath, C., Klessen, R. S., et al. 2025, Nature Astronomy, 9, 1195, doi: 10.1038/s41550-025-02551-5

Benítez-Llambay, P., Krapp, L., & Pessah, M. E. 2019, ApJS, 241, 25, doi: 10.3847/1538-4365/ab0a0e

Besard, T., Foket, C., & De Sutter, B. 2019, IEEE Transactions on Parallel and Distributed Systems, 30, 827, doi: 10.1109/TPDS.2018.2872064

Bezanson, J., Edelman, A., Karpinski, S., & Shah, V. B. 2017, SIAM Review, 59, 65, doi: 10.1137/141000671

Birnstiel, T., Dullemond, C. P., & Brauer, F. 2010, A&A, 513, A79, doi: 10.1051/0004-6361/200913731

Birnstiel, T., Fang, M., & Johansen, A. 2016, SSRv, 205, 41, doi: 10.1007/s11214-016-0256-1

Borges, R., Carmona, M., Costa, B., & Don, W. S. 2008, Journal of Computational Physics, 227, 3191, doi: 10.1016/j.jcp.2007.11.038

Branca, L., & Pallottini, A. 2024, A&A, 684, A203, doi: 10.1051/0004-6361/202449193

Brauer, F., Dullemond, C. P., & Henning, T. 2008, A&A, 480, 859, doi: 10.1051/0004-6361:20077759

Brio, M., & Wu, C. C. 1988, Journal of Computational Physics, 75, 400, doi: 10.1016/0021-9991(88)90120-9

Bruno, R., & Carbone, V. 2013, Living Reviews in Solar Physics, 10, 2, doi: 10.12942/lrsp-2013-2

Bryan, G. L., Norman, M. L., Stone, J. M., Cen, R., & Ostriker, J. P. 1995, Computer Physics Communications, 89, 149, doi: 10.1016/0010-4655(94)00191-4

Bryan, G. L., Norman, M. L., O'Shea, B. W., et al. 2014, ApJS, 211, 19, doi: 10.1088/0067-0049/211/2/19

Butsky, I. S., Redshaw, C., Lei, M., Clark, S. E., & Fielding, D. B. 2026, arXiv e-prints, arXiv:2606.11323. https://arxiv.org/abs/2606.11323

Byrne, S., Wilcox, L. C., & Churavy, V. 2021, Proceedings of the JuliaCon Conferences, 1, 68, doi: 10.21105/jcon.00068

Chen, M., Tworek, J., Jun, H., et al. 2021, arXiv e-prints, doi: 10.48550/arXiv.2107.03374

Churavy, V., Aluthge, D., Wilcox, L. C., et al. 2021, JuliaGPU/KernelAbstractions.jl: heterogeneous programming in Julia, Zenodo

Colella, P., & Woodward, P. R. 1984, Journal of Computational Physics, 54, 174, doi: 10.1016/0021-9991(84)90143-8

Drażkowska, J., Li, S., Birnstiel, T., Stammler, S. M., & Li, H. 2019, ApJ, 885, 91, doi: 10.3847/1538-4357/ab46b7

Dubrulle, B., Morfill, G., & Sterzik, M. 1995, Icarus, 114, 237, doi: 10.1006/icar.1995.1058

Dullemond, C. P., Ziampras, A., Ostertag, D., & Dominik, C. 2022, A&A, 668, A105, doi: 10.1051/0004-6361/202244218

Einfeldt, B. 1988, SIAM Journal on Numerical Analysis, 25, 294, doi: 10.1137/0725021

Epstein, P. S. 1924, Phys. Rev., 23, 710, doi: 10.1103/PhysRev.23.710

Estrada, P. R., Cuzzi, J. N., & Morgan, D. A. 2016, ApJ, 818, 200, doi: 10.3847/0004-637X/818/2/200

Eswaran, V., & Pope, S. B. 1988, Computers and Fluids, 16, 257, doi: 10.1016/0045-7930(88)90013-8

Evans, C. R., & Hawley, J. F. 1988, ApJ, 332, 659, doi: 10.1086/166684

Federrath, C., Klessen, R. S., Iapichino, L., & Beattie, J. R. 2021, Nature Astronomy, 5, 365, doi: 10.1038/s41550-020-01282-z

Fielding, D. B., Ripperda, B., & Philippov, A. A. 2023, ApJL, 949, L5, doi: 10.3847/2041-8213/accf1f

Flock, M., Nelson, R. P., Turner, N. J., et al. 2017, ApJ, 850, 131, doi: 10.3847/1538-4357/aa943f

Flock, M., Turner, N. J., Nelson, R. P., et al. 2020, ApJ, 897, 155, doi: 10.3847/1538-4357/ab9641

Flores-Rivera, L., Flock, M., & Nakatani, R. 2020, A&A, 644, A50, doi: 10.1051/0004-6361/202039294

Fryxell, B., Olson, K., Ricker, P., et al. 2000, ApJS, 131, 273, doi: 10.1086/317361

Fukuhara, Y., & Okuzumi, S. 2024, PASJ, 76, 708, doi: 10.1093/pasj/psae042

Gardiner, T. A., & Stone, J. M. 2005, Journal of Computational Physics, 205, 509, doi: 10.1016/j.jcp.2004.11.016

—. 2008, Journal of Computational Physics, 227, 4123, doi: 10.1016/j.jcp.2007.12.017

Godoy, W. F., Podhorszki, N., Wang, R., et al. 2020, SoftwareX, 12, 100561, doi: 10.1016/j.softx.2020.100561

Gottlieb, S., Ketcheson, D. I., & Shu, C.-W. 2009, Journal of Scientific Computing, 38, 251, doi: 10.1007/s10915-008-9239-z

Grassi, T., Bovino, S., Schleicher, D. R. G., et al. 2014, MNRAS, 439, 2386, doi: 10.1093/mnras/stu114

Grassi, T., Nauman, F., Ramsey, J. P., et al. 2022, A&A, 668, A139, doi: 10.1051/0004-6361/202039956

Grete, P., Glines, F. W., & O'Shea, B. W. 2021, IEEE Transactions on Parallel and Distributed Systems, 32, 85, doi: 10.1109/TPDS.2020.3010016

Grete, P., Dolence, J. C., Miller, J. M., et al. 2023, The International Journal of High Performance Computing Applications, 37, 465, doi: 10.1177/10943420221143775

Guillard, H., & Viozat, C. 1999, Computers and Fluids, 28, 63, doi: 10.1016/S0045-7930(98)00017-6

Harten, A., Lax, P. D., & van Leer, B. 1983, SIAM Review, 25, 35, doi: 10.1137/1025002

Hayashi, C. 1981, Progress of Theoretical Physics Supplement, 70, 35, doi: 10.1143/PTPS.70.35

Heiles, C., & Troland, T. H. 2005, The Astrophysical Journal, 624, 773, doi: 10.1086/428896

Ho, K. W., Li, H., & Li, S. 2024, ApJL, 975, L34, doi: 10.3847/2041-8213/ad8655

Ho, K. W., Yuen, K. H., Flauger, R., & Kritsuk, A. G. 2025, PhRvD, 112, L101302, doi: 10.1103/vhhn-33jw

Huang, P., & Bai, X.-N. 2022, ApJS, 262, 11, doi: 10.3847/1538-4365/ac76cb

Jimenez, C. E., Yang, J., Wettig, A., et al. 2024, arXiv e-prints, doi: 10.48550/arXiv.2310.06770

Ketcheson, D. I. 2010, Journal of Computational Physics, 229, 1763, doi: 10.1016/j.jcp.2009.11.006

Kochkov, D., Smith, J. A., Alieva, A., et al. 2021, Proceedings of the National Academy of Sciences, 118, e2101784118, doi: 10.1073/pnas.2101784118

Koyama, H., & Inutsuka, S.-i. 2002, ApJL, 564, L97, doi: 10.1086/338978

Krapp, L., Benítez-Llambay, P., Gressel, O., & Pessah, M. E. 2019, ApJL, 878, L30, doi: 10.3847/2041-8213/ab2596

Krapp, L., Garrido-Deutelmoser, J., Benítez-Llambay, P., & Kratter, K. M. 2024, ApJS, 271, 7, doi: 10.3847/1538-4365/ad14f9

Kritsuk, A. G., Ho, K. W., Yuen, K. H., & Flauger, R. 2026, in Proceedings of the 60th Rencontres de Moriond, Cosmology session. https://arxiv.org/abs/2605.06896

Kritsuk, A. G., Ustyugov, S. D., & Norman, M. L. 2017, New Journal of Physics, 19, 065003, doi: 10.1088/1367-2630/aa7156

Larrouturou, B. 1991, Journal of Computational Physics, 95, 59, doi: 10.1016/0021-9991(91)90253-H

Laune, J., Li, H., Li, S., et al. 2020, ApJL, 889, L8, doi: 10.3847/2041-8213/ab65c6

Lehmann, A., & Wardle, M. 2018, MNRAS, 476, 3185, doi: 10.1093/mnras/sty450

Lesur, G. R. J., Baghdadi, S., Wafflard-Fernandez, G., et al. 2023, A&A, 677, A9, doi: 10.1051/0004-6361/202346005

Li, Y.-P., Li, H., Li, S., et al. 2020, ApJL, 892, L19, doi: 10.3847/2041-8213/ab7fb2

Li, Z., Kovachki, N., Azizzadenesheli, K., et al. 2021, in International Conference on Learning Representations. https://arxiv.org/abs/2010.08895

Lin, M.-K., & Youdin, A. N. 2015, ApJ, 811, 17, doi: 10.1088/0004-637X/811/1/17

Liska, R., & Wendroff, B. 2003, SIAM Journal on Scientific Computing, 25, 995, doi: 10.1137/S1064827502402120

Liu, N. F., Lin, K., Hewitt, J., et al. 2024, Transactions of the Association for Computational Linguistics, 12, 157, doi: 10.1162/tacl_a_00638

Lombart, M., Bréhier, C.-E., Hutchison, M., & Lee, Y.-N. 2024, MNRAS, 533, 4410, doi: 10.1093/mnras/stae2039

Lombart, M., & Laibe, G. 2021, MNRAS, 501, 4298, doi: 10.1093/mnras/staa3682

Lu, L., Jin, P., Pang, G., Zhang, Z., & Karniadakis, G. E. 2021, Nature Machine Intelligence, 3, 218, doi: 10.1038/s42256-021-00302-5

Manger, N., Klahr, H., Kley, W., & Flock, M. 2020, MNRAS, 499, 1841, doi: 10.1093/mnras/staa2943

Mathis, J. S., Rumpl, W., & Nordsieck, K. H. 1977, ApJ, 217, 425, doi: 10.1086/155591

McNally, C. P., Lovascio, F., & Paardekooper, S.-J. 2021, MNRAS, 502, 1469, doi: 10.1093/mnras/stab112

Mignone, A. 2007, Journal of Computational Physics, 225, 1427, doi: 10.1016/j.jcp.2007.01.033

Mignone, A., Bodo, G., Massaglia, S., et al. 2007, ApJS, 170, 228, doi: 10.1086/513316

Minoshima, T., & Miyoshi, T. 2021, Journal of Computational Physics, 446, 110639, doi: 10.1016/j.jcp.2021.110639

Miyoshi, T., & Kusano, K. 2005, Journal of Computational Physics, 208, 315, doi: 10.1016/j.jcp.2005.02.017

Nakagawa, Y., Sekiya, M., & Hayashi, C. 1986, Icarus, 67, 375, doi: 10.1016/0019-1035(86)90121-1

Nelson, R. P., Gressel, O., & Umurhan, O. M. 2013, MNRAS, 435, 2610, doi: 10.1093/mnras/stt1475

Orszag, S. A., & Tang, C.-M. 1979, Journal of Fluid Mechanics, 90, 129, doi: 10.1017/S002211207900210X

Pal, A. 2023, Lux: Explicit Parameterization of Deep Neural Networks in Julia, Zenodo, doi: 10.5281/zenodo.7808904

Pfeil, T., Birnstiel, T., & Klahr, H. 2023, ApJ, 959, 121, doi: 10.3847/1538-4357/ad00af

Rackauckas, C., & Nie, Q. 2017, Journal of Open Research Software, 5, 15, doi: 10.5334/jors.151

Ramadhan, A., Wagner, G. L., Hill, C., et al. 2020, Journal of Open Source Software, 5, 2018, doi: 10.21105/joss.02018

Ranocha, H., Schlottke-Lakemper, M., Winters, A. R., et al. 2022, Proceedings of the JuliaCon Conferences, 1, 77, doi: 10.21105/jcon.00077

Rucska, J. J., & Wadsley, J. W. 2023, MNRAS, 526, 1757, doi: 10.1093/mnras/stad2855

Samaroo, J., Smirnov, A., Räss, L., Churavy, V., et al. 2026, JuliaGPU/AMDGPU.jl: AMD GPU (ROCm) programming in Julia, Zenodo, doi: 10.5281/zenodo.10040461

Schaffer, N., Yang, C.-C., & Johansen, A. 2018, A&A, 618, A75, doi: 10.1051/0004-6361/201832783

Schive, H.-Y., ZuHone, J. A., Goldbaum, N. J., et al. 2018, MNRAS, 481, 4815, doi: 10.1093/mnras/sty2586

Schmidt, W., Federrath, C., Hupp, M., Kern, S., & Niemeyer, J. C. 2009, A&A, 494, 127, doi: 10.1051/0004-6361:200809967

Schneider, E. E., & Robertson, B. E. 2015, ApJS, 217, 24, doi: 10.1088/0067-0049/217/2/24

Sedov, L. I. 1959, Similarity and Dimensional Methods in Mechanics (New York: Academic Press)

Shu, C.-W., & Osher, S. 1989, Journal of Computational Physics, 83, 32, doi: 10.1016/0021-9991(89)90222-2

Sod, G. A. 1978, Journal of Computational Physics, 27, 1, doi: 10.1016/0021-9991(78)90023-2

Stammler, S. M., & Birnstiel, T. 2022, ApJ, 935, 35, doi: 10.3847/1538-4357/ac7d58

Stoll, M. H. R., & Kley, W. 2014, A&A, 572, A77, doi: 10.1051/0004-6361/201424114

—. 2016, A&A, 594, A57, doi: 10.1051/0004-6361/201527716

Stone, J. M., Gardiner, T. A., Teuben, P., Hawley, J. F., & Simon, J. B. 2008, ApJS, 178, 137, doi: 10.1086/588755

Stone, J. M., & Norman, M. L. 1992, ApJS, 80, 753, doi: 10.1086/191680

Stone, J. M., Tomida, K., White, C. J., & Felker, K. G. 2020, ApJS, 249, 4, doi: 10.3847/1538-4365/ab929b

Stone, J. M., Mullen, P. D., Fielding, D., et al. 2026, ApJS, 283, 27, doi: 10.3847/1538-4365/ae3717

Taylor, G. 1950, Proceedings of the Royal Society of London Series A, 201, 159, doi: 10.1098/rspa.1950.0049

Taylor, G. I., & Green, A. E. 1937, Proceedings of the Royal Society of London Series A, 158, 499, doi: 10.1098/rspa.1937.0036

Testi, L., Birnstiel, T., Ricci, L., et al. 2014, in Protostars and Planets VI, ed. H. Beuther, R. S. Klessen, C. P. Dullemond, & T. Henning, 339, doi: 10.2458/azu_uapress_9780816531240-ch015

Teyssier, R. 2002, A&A, 385, 337, doi: 10.1051/0004-6361:20011817

Toro, E. F. 2009, Riemann Solvers and Numerical Methods for Fluid Dynamics: A Practical Introduction, 3rd edn. (Berlin: Springer), doi: 10.1007/b79761

Tóth, G. 2000, Journal of Computational Physics, 161, 605, doi: 10.1006/jcph.2000.6519

Trott, C. R., Lebrun-Grandié, D., Arndt, D., et al. 2022, IEEE Transactions on Parallel and Distributed Systems, 33, 805, doi: 10.1109/TPDS.2021.3097283

Utkarsh, U., Churavy, V., Ma, Y., et al. 2024, Computer Methods in Applied Mechanics and Engineering, 419, 116591, doi: 10.1016/j.cma.2023.116591

van Leer, B. 1974, Journal of Computational Physics, 14, 361, doi: 10.1016/0021-9991(74)90019-9

Wibking, B. D., & Krumholz, M. R. 2022, MNRAS, 512, 1430, doi: 10.1093/mnras/stac439

Wolfire, M. G., Hollenbach, D., McKee, C. F., Tielens, A. G. G. M., & Bakes, E. L. O. 1995, ApJ, 443, 152, doi: 10.1086/175510

Wolfire, M. G., McKee, C. F., Hollenbach, D., & Tielens, A. G. G. M. 2003, ApJ, 587, 278, doi: 10.1086/368016

Yang, C.-C., & Zhu, Z. 2021, MNRAS, 508, 5538, doi: 10.1093/mnras/stab2959

Yang, J., Chen, Z., & Bai, X.-N. 2026, arXiv e-prints, arXiv:2607.13740. https://arxiv.org/abs/2607.13740

Yang, J., Jimenez, C. E., Wettig, A., et al. 2024, arXiv e-prints, doi: 10.48550/arXiv.2405.15793

Youdin, A. N., & Goodman, J. 2005, ApJ, 620, 459, doi: 10.1086/426895

Youdin, A. N., & Lithwick, Y. 2007, Icarus, 192, 588, doi: 10.1016/j.icarus.2007.07.012

Zhang, X., & Shu, C.-W. 2010, Journal of Computational Physics, 229, 8918, doi: 10.1016/j.jcp.2010.08.016

Zhu, Z., & Yang, C.-C. 2021, MNRAS, 501, 467, doi: 10.1093/mnras/staa3628

Zweibel, E. G., & Yamada, M. 2009, Annual Review of Astronomy and Astrophysics, 47, 291, doi: 10.1146/annurev-astro-082708-101726